A Hierarchical Control Strategy With Fault Ride-Through Capability for Variable Frequency Transformer

A Hierarchical Control Strategy With Fault Ride-Through Capability for Variable Frequency Transformer

Bharath Babu Ambati, Parag Kanjiya, Vinod Khadkikar, *Member, IEEE*, Mohamed Shawky El-Moursi, *Member, IEEE*, and James L. Kirtley Jr., *Fellow, IEEE*

***Abstract*—A variable frequency transformer (VFT) is being considered as a new alternative to the classical back-to-back high voltage direct current (HVDC) system for interconnection of two asynchronous networks. The VFT is a retrospective form of frequency converter using the wound rotor induction machine (WRIM), which converts the constant frequency input into a variable frequency output. The prime objective of VFT is to achieve controlled bidirectional power transfer between the two asynchronous networks. This paper presents a detailed working principle of VFT technology and proposes a new hierarchical control strategy for establishing the VFT connection with two power systems to achieve bidirectional power transfer between them. Also, to restrict the grid fault propagation from one side of the VFT to the other side, a series dynamic braking resistor based fault ride-through (FRT) scheme is proposed. The performance of the VFT during synchronization process, steady-state, dynamic, and the grid fault conditions is evaluated using the real-time hardware in-loop (HIL) system. The plant is simulated in real time using OPAL-RT real-time simulator while the control algorithm is implemented in digital signal processor to carry out HIL study. All the important results supporting the effectiveness of the proposed control strategy and FRT scheme are discussed.**

***Index Terms*—Fault propagation, hierarchical control, power flow control, rotating transformer, series dynamic breaking resistor (SDBR), variable frequency transformer (VFT).**

I. Introduction

In GENERAL, the interconnection of two different power networks with controlled power transfer capability can be achieved by a synchronous tie using a phase-shifting transformer or by an asynchronous tie using classical back-to-back high voltage direct current (HVDC) link. In the modern power systems, establishing a synchronous tie between two power networks would be a challenging task especially when one or both the networks experience a slight variation in their frequencies [1]. Moreover, the use of phase-shifting transformers in synchronous ties suffers from the drawbacks such as slow and step-wise controls [2]. This further causes wear and tear of tap changer contacts. Although, the use of power electronic controlled phase-shifting transformer can eliminate these drawbacks, they introduce additional problems such as harmonics, resonance, vulnerability to voltage surges, and reduced overloading capability due to their low thermal time constant [2], [3]. On the other hand, a back-to-back HVDC link can be established between any two power networks to achieve the controlled power flow between them. A line commutated converter (LCC)-based HVDC link suffers with the bottlenecks such as large reactive power requirements, lower thermal time constant, and lack of inertia for natural damping. Whereas, the voltage source converter (VSC)-based HVDC link can control the reactive power unlike LCC-based HVDC link. But, the inertia contribution and frequency response are still the challenges for HVDC technologies. Alternatively, the use of variable frequency transformer (VFT) for asynchronous interconnection can improve the system inertia and frequency control.

The VFT was first developed by General Electric Company in 2004 to achieve the interconnection of two different power networks [2]. A VFT is a controllable bidirectional power transfer device between the two asynchronous power networks that consists of wound rotor induction machine (WRIM) and a dc motor drive [2]. The presence of rotating mass (of both WRIM and dc motor) adds inertia to the power systems and thereby improves the stability during system disturbances. The VFT offers significant benefits over the widely installed LCC–HVDC link [4]–[6], mainly, lower reactive power requirements, harmonic-free power transfer, and higher system stability.

Basic concept and design aspects of 100 MW VFT is presented in [2]. The performance of VFT during steady-state, dynamic, and transient conditions is evaluated using simulation studies in [7]–[12]. In [13], the offshore wind park is connected to the grid through VFT to reduce the power fluctuations using the PID damping torque controller of the dc motor drive. Moreover, the use of brushless doubly fed induction machine (BDFIM) with squirrel cage rotor as alternative VFT configuration is reported in [6]. In which, the dual stator winding with different pole numbers with a ratio of 1:3 is used to avoid space harmonics concerns. The operating performance and maintenance of VFT is discussed in [15] and [16].

The steady-state analysis of the VFT is well established in the literature [2]–[12], but the problem of fault propagation and the fault ride-through (FRT) enhancement is not addressed so far. As

Manuscript received October 28, 2013; revised February 27, 2014 and May 19, 2014; accepted June 21, 2014. Paper no. TEC-00638-2013.

B. B. Ambati, P. Kanjiya, and V. Khadkikar are with the Center for Energy, Masdar Institute of Science and Technology, Abu Dhabi, 54224, UAE (e-mail: bambati@masdar.ac.ae; pkanjiya@masdar.ac.ae; vkhadkikar@masdar.ac.ae).

M. S. El-Moursi and J. L. Kirtley Jr. are with the Department of Electrical Engineering and Computer Science, Massachusetts Institute of Technology, Cambridge, MA 02139 USA. (e-mail: melmoursi@masdar.ac.ae; kirtley@mit.edu).

Color versions of one or more of the figures in this paper are available online at http:ieeexplore.ieee.org.

Digital Object Identifier 10.1109/TEC.2014.2336981

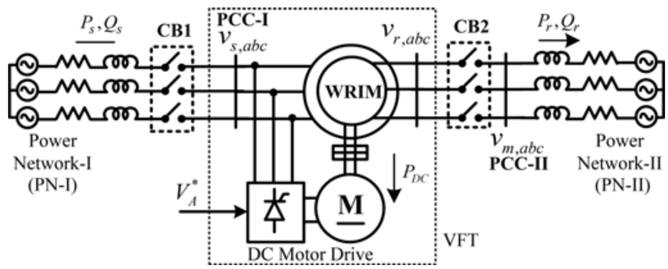

Fig. 1. VFT system configuration.

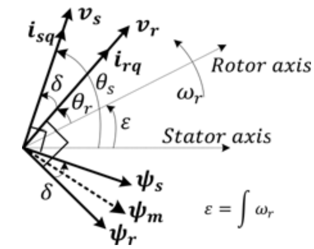

Fig. 2. Stator and rotor fluxes and voltages in VFT.

the fault propagation is a critical issue that affects power system reliability and security, the FRT protection schemes should be deployed in the VFT. In addition to that, the detailed control strategy for VFT is not presented in the literature.

This paper presents a detailed hierarchical control strategy for the VFT to achieve the following functions: establish a connection between two power systems, power transfer control, and FRT operation. Furthermore, a new topology of VFT comprising a series dynamic braking resistor (SDBR) is proposed to enhance the FRT capability. A number of states are defined for VFT operation to effectively connect it, operate it in steady state, and protect it during the grid faults. The proposed control strategy and VFT configuration are validated using real-time hardware in-loop (HIL) simulation. The plant is simulated in real time using OPAL-RT real-time simulator while the control algorithm is implemented in dSPACE-1103 to carry out HIL study.

II. Variable Frequency Transformer

Fig. 1 shows the VFT system configuration that consists of a WRIM mechanically coupled with a dc motor drive. The three-phase stator and rotor windings of WRIM are connected to two asynchronous power networks namely power network-I (PN-I) and power network-II (PN-II) as illustrated in Fig. 1. The frequencies and/or phase angles of both PN-I (f_s and θ_s) and PN-II (f_m and θ_m) could be different in actual application.

To connect the stationary VFT to the PN-I and PN-II simultaneously, the frequencies (f_s and f_m) and phase angles (θ_s and θ_m) should be identical. It is difficult to achieve this condition in practical system. Therefore, the following approach is deployed with the VFT to make this asynchronous interconnection.

1) Connect the PN-I directly to the stator side of the VFT (by closing CB1) while keeping the rotor stationary and circuit breaker CB2 open.
2) Measure the frequency f_r and phase angle θ_r of the voltage induced in the rotor windings ($v_{r,\mathrm{abc}}$) at the terminals of CB2 (when the rotor is stationary, $f_r = f_s$ and $\theta_r = \theta_s$).
3) Measure the frequency f_m and phase angle θ_m of PN-II voltage ($v_{m,\mathrm{abc}}$) available on the other side of CB2.
4) Control the rotor speed to change f_r by using the dc motor drive to achieve $f_r = f_m$.
5) Adjust the rotor position (θ_r) using the dc motor drive to make $\theta_r = \theta_m$.
6) The synchronization between voltages $v_{r,\mathrm{abc}}$ and $v_{m,\mathrm{abc}}$ is achieved by steps 4 and 5, then the CB2 can be closed to establish the interconnection between both networks through VFT.

Here onwards, the points 4 and 5 are referred as frequency matching and phase angle matching, respectively. A control algorithm required to control the dc motor drive in VFT is developed in Section V.

III. VFT Concept and Power Flow

Based on the existing literature, the working principle and the active and reactive power flow through the VFT have not been discussed in detail. In addition to that, FRT operation and protection strategy have not been addressed. Hence, the detailed VFT model is developed to study all the operational aspects for steady-state, dynamic, and transient conditions.

A. Active Power Transfer and Control

The synchronization procedure described in the previous section is used to connect both power networks in Fig. 1. Consequently, both the stator and rotor fluxes will be in synchronism irrespective of the rotor speed with a specific phase angle difference represented as load angle (δ). The controllability of this load angle δ and its effect on active power transfer between both networks is analyzed in this subsection.

The stator and rotor voltage vectors and the respective flux vectors referred to stator are shown in Fig. 2. The instantaneous stator flux ($\boldsymbol{\psi}_\mathbf{s}$), air-gap flux ($\boldsymbol{\psi}_\mathbf{m}$) and rotor flux ($\boldsymbol{\psi}_\mathbf{r}$) vectors in the stationary reference frame can be expressed as

$$\boldsymbol{\psi}_\mathbf{s} = L_s \mathbf{i}_\mathbf{s} + L_m \left(\mathbf{i}_\mathbf{r} \mathbf{e}^{\mathrm{j}\varepsilon}\right) \quad (1)$$

$$\boldsymbol{\psi}_\mathbf{m} = L_m \left(\mathbf{i}_\mathbf{s} + \left(\mathbf{i}_\mathbf{r} \mathbf{e}^{\mathrm{j}\varepsilon}\right)\right) \quad (2)$$

$$\boldsymbol{\psi}_\mathbf{r} = L_r \mathbf{i}_\mathbf{r} + L_m \left(\mathbf{i}_\mathbf{s} \mathbf{e}^{-\mathrm{j}\varepsilon}\right) \quad (3)$$

where L_s, L_r, and L_m represent the equivalent stator, rotor, and mutual inductances referred to stator side; $\mathbf{i}_\mathbf{s}$ and $\mathbf{i}_\mathbf{r}$ are the stator and rotor currents, respectively. ε is the angular displacement between the stator and rotor fluxes and ω_r is the angular (mechanical) speed of the rotor.

From Fig. 2 and (1)–(3), the expression for the electromagnetic torque (T_e) can be obtained as [14]

$$T_e = \frac{2}{3}\frac{p}{2}\frac{L_m}{L_s L_r}\mathrm{Im}\left[\boldsymbol{\psi}_\mathbf{s}\boldsymbol{\psi}_\mathbf{r}^*\right] = \frac{2}{3}\frac{p}{2}\frac{L_m}{L_s L_r}\left|\boldsymbol{\psi}_\mathbf{s}\right|\left|\boldsymbol{\psi}_\mathbf{r}^*\right|\sin\delta. \quad (4)$$

The aforementioned relationship shows that the electromagnetic torque developed is a cross product of stator and rotor fluxes, i.e., the product of magnitudes of $\boldsymbol{\psi}_{\mathbf{s}}$, $\boldsymbol{\psi}_{\mathbf{r}}$, and the sine of the angle δ between both the fluxes. On the other hand, general expression for the developed electromagnetic torque in any reference frame (*d–q* or $\propto$–β) can be written as

$$T_e = k\boldsymbol{\psi}_{\mathbf{m}} i_q \tag{5}$$

where k is the torque constant, and i_q is component of current vector in quadrature with $\boldsymbol{\psi}_{\mathbf{m}}$. Here, the quadrature component of current refers to stator/rotor current as the angle between $\boldsymbol{\psi}_{\mathbf{m}}$ and $\boldsymbol{\psi}_{\mathbf{s}}$ or $\boldsymbol{\psi}_{\mathbf{m}}$ and $\boldsymbol{\psi}_{\mathbf{r}}$ is very small.

From the basic integral relation between the flux and voltage, a current that is in quadrature with the flux is in-phase or out-of-phase with the voltage and hence responsible for active power flow. In general, the VFT is connected between the two power systems whose voltages are fairly constant and hence the magnitudes of $\boldsymbol{\psi}_{\mathbf{s}}$, $\boldsymbol{\psi}_{\mathbf{r}}$, and $\boldsymbol{\psi}_{\mathbf{m}}$ can be treated as constants. Therefore, from (4) and (5) it can be deduced that the torque developed/imposed on the rotor is proportional to $'\mathrm{Sin}\,\delta'$ and active component of stator/rotor current. If the displacement angle ε in Fig. 2 is changed by applying external torque through the dc motor drive, the angle δ and hence electromagnetic torque developed in the WRIM will change according to (4). Consequently, it changes the active current (i_q) as per (5). It can be observed that the active current variation is in proportion to δ (as the δ is very small, $\mathrm{Sin}\,\delta \approx \delta$), which is analogous to a series inductor behavior. The generalized active power flow through the series inductor is expressed by

$$P = \frac{V_s V_r}{X_s} \sin\delta. \tag{6}$$

Therefore, for the case of VFT, considering a stator to rotor turns ratio of 1:1, and neglecting the losses in the system, the active power transfer (P_{VFT}) in terms of the stator and rotor voltages, from Fig. 2, can be written as

$$P_{\mathrm{VFT}} = \frac{V_s V_r}{X_s} \sin\left(\theta_s - (\theta_r + \varepsilon)\right) \tag{7}$$

where V_s and θ_s are the *rms* stator voltage and its phase angle, respectively; V_r and θ_r are the *rms* rotor voltage and its phase angle, respectively; and X_s is the series equivalent inductive reactance offered by the VFT. The term ε in (7) is the time integral of ω_r to be controlled by the dc motor drive.

By neglecting the leakage reactance and magnetizing current (i.e., power factors close to unity) of the VFT [2], the mechanical power handled by the dc motor drive can be expressed as

$$P_{\mathrm{dc}} = P_s - P_r = V_s I_s - V_r I_r \tag{8}$$

where I_s and I_r are the *rms* values of the active component of stator and rotor currents, respectively. Considering volt/hertz/turn and MMF balance between the stator and rotor windings of the VFT, the above expression can be rewritten as [2]

$$P_{\mathrm{dc}} = V_s I_s - \left(\frac{V_s}{N_s f_s} N_r f_r\right)\left(\frac{I_s N_s}{N_r}\right) = V_s I_s \left(1 - \frac{f_r}{f_s}\right) \tag{9}$$

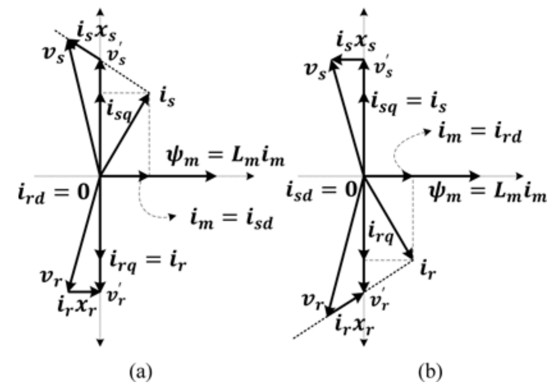

Fig. 3. Reactive power flow concept in the VFT. (a) $\nu_s > \nu_r$ (b) $\nu_s < \nu_r$

where N_s and N_r are the number of turns in the stator and rotor windings of VFT, respectively. From (9), it is clear that the power absorbed by the dc motor drive is a function of frequency difference between both the power networks and the power being transferred through the VFT. Also, from (9), the torque expression for the dc motor can be written as

$$T_{\mathrm{dc}} = \frac{P_{\mathrm{dc}}}{\omega_r} = \frac{V_S I_S \left(1 - \frac{f_r}{f_s}\right)}{2\pi \dfrac{120\,(f_s - f_r)/p}{60}} = \frac{p}{2}\frac{V_S I_S}{2\pi f_s} \tag{10}$$

where p is number of poles in the WRIM. From (10), it can be noticed that the torque developed by the dc motor drive is independent of speed of rotation. Assuming the constant stator voltage in (10), it can be noticed that by changing the torque applied through dc motor drive, the stator active current (I_S) can be changed. This proves the correlation between torque applied by dc motor drive and active current transferred through VFT according to (5). A simple armature voltage controlled four quadrant dc drive can be employed to regulate the torque produced by the dc motor and thereby active power transfer.

B. Reactive Power Transfer

Stator and rotor reactive currents (i_{sd} and i_{rd}) of VFT may consists of two components: 1) the magnetizing current required for VFT operation (i_m); and 2) the reactive current transferred between the two networks. The amount of reactive current supplied/absorbed by each network is dependent on the voltage magnitudes at the stator (PCC-I) and rotor (PCC-II) terminals. Regardless of slight difference in grid voltages on both sides, the VFT maintains the volt/hertz/turn balance between induced stator (v_s') and rotor (v_r') voltages by circulating the appropriate amount of reactive current between both the networks.

Two different cases are demonstrated to show the reactive power flow dependency on the voltage magnitudes on both sides of VFT as illustrated in Fig. 3. The stator and rotor resistances are neglected and it is assumed that the active current transferred between the stator and rotor is constant ($i_{\mathrm{sq}} = -i_{\mathrm{rq}}$) throughout the operation. Fig. 3(a) represents the case where the stator voltage is slightly higher than the rotor voltage referred to stator side (i.e., $v_s > v_r$). Assuming the induced stator voltage (v_s')

is constant, any increase in v_s causes increase in i_s according to $v_s = v_s' + i_s x_s$. For the fixed active power transfer, active current (i_{sq}) is constant and hence reactive current (i_{sd}) has to increase in order to accommodate the change in i_s. In Fig. 3(a), the stator voltage magnitude is considered such that whole magnetizing current (i_m) required for VFT operation comes from the stator (i.e., $i_m = i_{\mathrm{sd}}$ and $i_{\mathrm{rd}} = 0$). Thus, further increase in the stator voltage magnitude leads to i_{sd} higher than i_m, that makes $i_{\mathrm{rd}} = -(i_{\mathrm{sd}} - i_m)$ which is the net reactive current transferred from PN-I to PN-II through VFT. Accordingly, any reduction in stator voltage magnitude drives the stator and rotor sides to supply the required magnetizing current i_m for VFT operation.

The vector diagram corresponding to the case where full magnetizing current is drawn from the rotor side due to higher rotor voltage is shown in Fig. 3(b). Similar to the aforementioned case, any further increase in the rotor voltage in Fig. 3(b) leads to reactive power flow from PN-II to PN-I.

It is obvious that the reactive power flow into/through VFT is uncontrolled and is mostly dependent on the terminal voltage magnitudes of v_s and v_r. The VFT requires a fixed amount of reactive power to meet the constant magnetization demand regardless of the amount and/or direction of active power transfer. The stator and rotor currents through VFT can be obtained from the steady-state equivalent circuit for particular voltage conditions and reactive powers can be computed as

$$Q_s = |\boldsymbol{\nu}_s|\,|\mathbf{i}_{\mathrm{sd}}| = \mathrm{Im}\,[\boldsymbol{\nu}_s i_s^*] \tag{11}$$

$$Q_r = |\boldsymbol{\nu}_r|\,|\mathbf{i}_{\mathrm{rd}}| = \mathrm{Im}\,[\boldsymbol{\nu}_r i_r^*]\,. \tag{12}$$

For the power flow directions shown in Fig. 1, the reactive power absorbed by VFT (Q_m) at any operating condition is the difference between stator and rotor reactive powers, i.e.,

$$Q_m = Q_s - Q_r. \tag{13}$$

IV. SDBR Protection Scheme for VFT

As discussed in the previous section, during the steady-state operation, VFT is analogous to a series inductor. Therefore, during a voltage dip resulted from the grid fault in one of the power networks, the other network is forced to supply a large fault currents. This indicates the propagation of a fault from the faulted network to the healthy power network through VFT. This fault propagation phenomenon associated with VFT has not been discussed in the literature. To demonstrate the problems associated with the fault propagation, a fault condition is considered at PN-II as shown in Fig. 1. This grid fault (or voltage dip) has the following consequences unless appropriate protective measures are taken:

1) large fault currents from the stator side;
2) temporary disconnection of VFT due to CB1 opening;
3) oscillations/instability in PN-I due to system dynamics;
4) slow post fault recovery due to VFT disconnection;
5) possible requirement of VFT resynchronization;
6) damage to VFT windings in the event of protection failure.

This paper introduces an appropriate FRT scheme within the VFT system using SDBR to overcome the issue of fault propagation as shown in Fig. 4. The SDBR protection scheme is identified as simple and economic solution for enhancing the FRT capability and transient performance of VFT in response to symmetrical and asymmetrical grid faults. It can be noted that, four different combinations of power flow direction (PN-I to PN-II or PN-II to PN-I) and the grid fault (in PN-I or PN-II) are possible in the VFT. The SDBR scheme that can prevent the fault propagation in all four possible cases can be designed using a simple approach by considering a power flow from PN-I to PN-II and the grid fault in PN-II as described in the following.

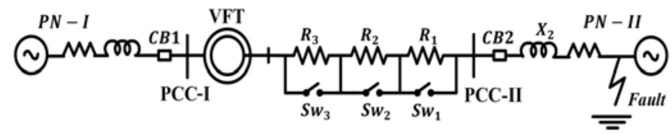

Fig. 4. Single line diagram of SDBR protection scheme for VFT.

A. Series Resistance Selection

According to the design criteria, the SDBR should limit the fault current by acting as a voltage booster against the voltage in PN-II at the rotor terminals and protect the healthy network (PN-I) connected to the stator terminal. To be able to work with various levels of grid faults (based on magnitudes of voltage dip), the SDBR should have different combination of resistors. The SDBR with n resistors can realize $(2^n - 1)$ combinations of resistances. The maximum and minimum possible resistance values of SDBR should be selected based on the following two scenarios.

1) Voltage Dip Operation: During the most severe grid fault, the voltage appears on the rotor terminals should be higher than the minimum allowable rotor voltage (V_{r_min}). The maximum value of series resistance ($R_{\mathrm{SDBR\_max}} = R_1 + R_2 + \ldots + R_n$) required to achieve this during the worst case voltage dip can be calculated using the following:

$$V_{\mathrm{fault\_min}} + \frac{P_{\mathrm{rated}}}{3V_{r\_\mathrm{min}}} R_{\mathrm{SDBR\_max}} \geq kV_{r\_\mathrm{min}} \tag{14}$$

where $V_{\mathrm{fault\_min}}$ is the lowest possible grid voltage (at PCC-II) during the grid fault on PN-II, P_{rated} is the rated power transfer capability of VFT, and k is safety margin (>1) to take care of the lagging power factor.

2) Overvoltage Protection: The designed SDBR should not cause the overvoltage across the rotor terminals in any case such as small voltage dips. The minimum value of series resistance ($R_{\mathrm{SDBR\_min}}$) that prevents the rotor overvoltage can be computed from the following equation:

$$V_{\mathrm{fault\_max}} + \frac{P_{\mathrm{rated}}}{3V_{r\_\mathrm{rated}}} R_{\mathrm{SDBR\_min}} \leq 3V_{r\_\mathrm{rated}} \tag{15}$$

where $V_{\mathrm{fault\_max}}$ is the grid voltage (at PCC-II) during the minor voltage dip that can trigger the SDBR. For the present case of SDBR with three resistances, the value of different resistors can be calculated from the maximum and minimum values of

SDBR resistances obtained through (14) and (15) as follows:

$$\begin{aligned} R_1 &= R_{\text{SDBR\_min}} \\ R_2 &= \frac{1}{3}\left[R_{\text{SDBR\_max}} - R_{\text{SDBR\_min}}\right] \\ R_3 &= \frac{2}{3}\left[R_{\text{SDBR\_max}} - R_{\text{SDBR\_min}}\right]. \end{aligned} \tag{16}$$

B. Static AC Switch Selection

Three SDBR resistors can be inserted into the circuit by controlling the static ac switches Sw_1, Sw_2, and Sw_3, respectively. Three ac switches are required for switching the resistors (R_1, R_2, and R_3) in each phase as per Fig. 4. Therefore, a total of nine resistors (R_1, R_2, and R_3 for each phase) and nine ac switches are deployed to realize the SDBR protection scheme.

The current rating of ac switches in SDBR scheme should be equal to the rated VFT current as they remain closed during the steady-state operation. And, the voltage rating of the switches should be equal to the product of rated VFT current and corresponding resistor value. It is worthy to note that the switching losses are absent (as switches are always closed) during the steady-state operation and therefore, the switches with low conduction losses are preferred for this SDBR scheme.

The ac switches can be realized using either antiparallel thyristors (low cost) or antiseries IGBTs (high cost). The choice of the switch depends on the speed requirement of resistor insertion during the fault. The antiparallel thyristor switch has a maximum of half cycle delay in operation as it breaks the current at next zero crossing while, antiseries IGBT switch can break the current instantaneously.

The WRIM in the VFT system possesses large thermal time constant and can easily handle the current surge resulted from the delay in ac switch opening. Therefore, the low cost antiparallel thyristor switches are used as ac switches in SDBR protection scheme.

V. Proposed Hierarchical Control Strategy

This section describes the overall control of VFT and SDBR. The dc motor drive is the only controllable device in a VFT system that can regulate the power flow between two power networks. However, as highlighted in the previous section SDBR is an additional controllable device for the restriction of fault propagation. A comprehensive hierarchical strategy, with all the necessary controls, is proposed in three operational stages.

When the stator is directly connected to PN-I and circuit breaker CB2 is open, the dc motor drive is to be controlled to achieve the frequency matching ($f_r = f_m$) and phase angle matching ($\theta_r = \theta_m$). This part of control is realized in first two stages (Stage-I and Stage-II) of the proposed hierarchical control. Once the connection is established between both the power networks through VFT, the power transfer control is carried out in Stage-III.

The control block diagram depicting these three stages of the proposed hierarchical control is shown in Fig. 5. A four-quadrant armature voltage control method is employed for dc drive in the proposed hierarchical control. The changeover from one stage to another is realized using the states S_1, S_2, and S_3 as illustrated in Fig. 5 with the predefined hierarchy depicted in Fig. 6. The control of SDBR protection scheme is also incorporated in the flow chart of Fig. 6. The objective and control of VFT in each stage of hierarchical control is discussed in the following subsections.

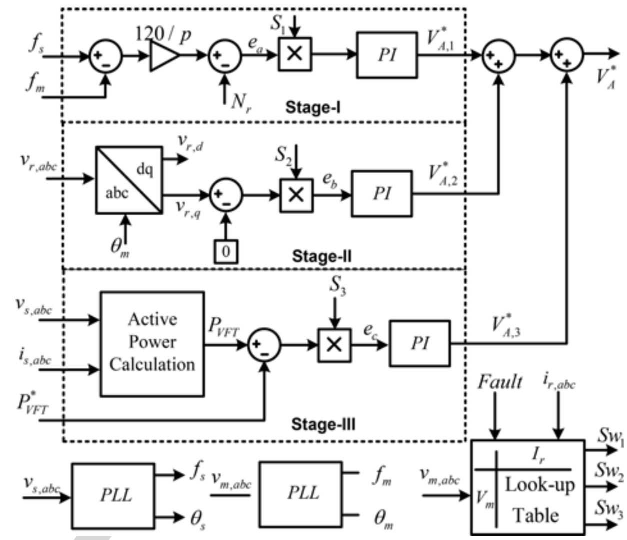

Fig. 5. Proposed hierarchical control strategy for synchronization and power transfer control in VFT.

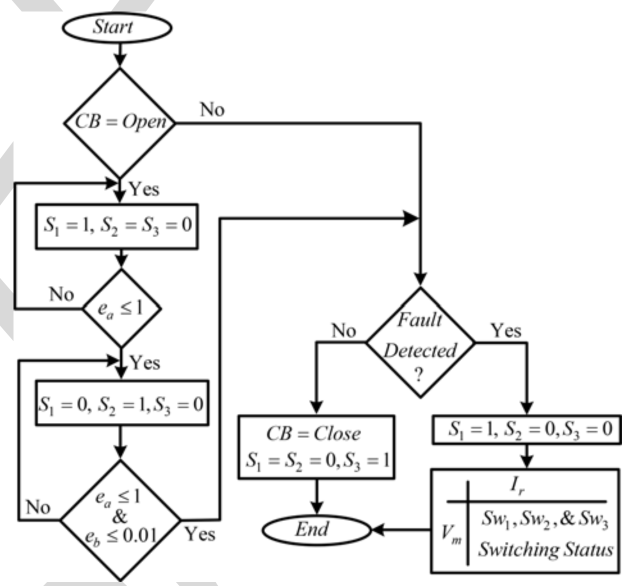

Fig. 6. Flow chart for hierarchical control strategy and SDBR control.

A. Stage-I: Frequency Matching

Initially when the stator of WRIM is connected to PN-I, the rotor is stationary and CB2 is open, the command $S_1 = 1$ is issued to start the frequency matching stage. At this condition the frequency of rotor voltage f_r has to be changed from $f_r = f_s$ to $f_r = f_m$. To achieve this desired frequency change, the equivalent rotor speed at which the rotor of VFT should be driven by dc motor drive is

$$N_r^* = \frac{120\,(f_s - f_m)}{p}. \tag{17}$$

The reference (N_r^*) and actual (N_r) speeds are compared, and the error, e_a, is processed through the PI controller to generate the necessary armature voltage ($V_{A,1}^*$) for the armature controlled dc motor drive (shown in Stage-I of Fig. 5). Once, the mean of absolute speed error (e_a) goes below 1 r/min, S_1 becomes low and S_2 becomes high as shown in the flow chart given in Fig. 6. Thereafter, high state of S_2 enables the next stage of hierarchical control.

B. Stage-II: Phase Angle Matching

Subsequent to the frequency matching, the next objective is to achieve the phase angle matching between $v_{r,\mathrm{abc}}$ and $v_{m,\mathrm{abc}}$ (i.e., $\theta_r = \theta_m$). Applying *abc–dq* transformation on the measured rotor voltages ($v_{r,\mathrm{abc}}$) using the phase angle (θ_m) of PN-II voltage ($v_{m,\mathrm{abc}}$), obtained from the phase locked loop (PLL), gives the direct ($v_{r,d}$) and quadrature ($v_{r,q}$) components of rotor voltages referred to PN-II voltage phasor. When the rotor voltage phase angle (θ_r) is exactly equal to θ_m, the computed $v_{r,q}$ becomes zero. In other words, by making $v_{r,q} = 0$, the phase angles can be matched (θ_r and θ_m). To achieve this, a PI controller is used over the $v_{r,q}$ for generating the necessary armature voltage ($V_{A,2}^*$) to change the rotor position (shown in Stage-II of Fig. 5). As soon as the mean of the absolute phase angle error (e_b or $v_{r,q}$) goes below certain margin (say 1%), S_2 goes low indicating the completion of Stage-II (shown in Fig. 6).

After frequency and phase angle matching are completed, the CB2 closes to establish the connection between both the networks through VFT. Subsequently, S_3 goes high to enable the power transfer controller.

C. Stage-III: Power Transfer Control

Actual power transfer (P_{VFT}) from PN-I to PN-II is measured on the stator side of VFT and compared with the reference power (P_{VFT}^*). The error is passed through the PI controller to generate the necessary armature voltage ($V_{A,3}^*$) and thus to control the torque developed by the dc motor drive (T_{dc}). The torque produced by dc motor drive dynamically adjusts the angle ε to achieve the desired load angle δ that makes $P_{\mathrm{VFT}}^* = P_{\mathrm{VFT}}$ as per (7).

The reference armature voltage (V_A^*) for the dc motor drive is expressed as follows:

$$V_A^* = V_{A,1}^* + V_{A,2}^* + V_{A,3}^*. \tag{18}$$

During the power transfer control, any change in the networks frequencies forces the rotor to adjust its speed according to (17).

D. SDBR-Based Fault Ride-Through Control

The SDBR control and fault detection is integrated in the hierarchical control strategy as shown in Fig. 6. When the grid fault occurs, the power transfer control should saturate at its prefault value to avoid rotor acceleration in response to fault conditions. This is achieved by forcing $S_3 = 0$ to keep the corresponding PI controller output at its prefault value. Whereas, the command $S_1 = 1$ (frequency matching loop) is reissued during the fault to damp out the rotor oscillations by controlling the torque of the dc motor drive. Simultaneously, there is a need to insert a suitable combination of resistors in SDBR that prevent the fault propagation from the faulted network to the healthy network. This is obtained using a two-dimensional (2 D) lookup table based on VFT current and fault voltage magnitudes. The output of lookup table is status of switches Sw_1, Sw_2, and Sw_3 that inserts a appropriate combination of R_1, R_2, and R_3. The switches Sw_1, Sw_2, and Sw_3 of each phase are simultaneously controlled for balanced faults while they are controlled independently for each phase during the unbalance faults. After the fault is cleared, the power transfer controller is reactivated to maintain the power transfer control by giving the control signals $S_1 = S_2 = 0, S_3 = 1$. The coordination between the three stages of the proposed hierarchical control and the proposed SDBR control is shown in Fig. 6.

VI. Real-Time Hardware In-Loop Validation

The proposed hierarchical control strategy and SDBR scheme for VFT are verified using a real-time HIL implementation. The control algorithm is implemented in the digital signal processor (DSP) board, DS1103 from dSPACE at a step size of 50 μs. The plant (VFT test system and SDBR scheme) is emulated using the OPAL-RT real-time simulator. The communication between the controller and the plant is carried out through ADC and DAC ports of DS1103 and OPAL-RT.

Due to high torque requirement by the VFT system during low speed operations, a geared dc motor with a mechanical gear of ratio 1:10 is used instead of conventional dc motor. The use of geared dc motors can significantly reduce the size of the dc motor during the actual applications of VFT. The system specifications and the machine parameters of VFT test system are given in Table I.

A. Steady-State Performance

The performance of VFT system during the three stages of proposed hierarchical control is shown in Figs. 7–9. All the results are given in per unit values with $1\ \mathrm{div} = 1$ p.u. The dc motor drive power P_{dc} and speed N_r are represented on the basis of 100 W and 60 r/min for a better visualization of their dynamics. The PN-I operates at 400 V/50 Hz while the PN-II operates at 392 V/49 Hz. The effectiveness of each stage of hierarchical control and the transition from one stage to another can be seen from Fig. 7. When VFT is stationary the frequency f_r of the induced rotor voltage ($v_{r,a}$) is 50 Hz while the frequency f_m of PN-II voltage ($v_{m,a}$) is 49 Hz. As highlighted in Section II, to close the circuit breaker CB2, synchronization should be established between the $v_{r,a}$ and $v_{m,a}$. Therefore in Stage-I, with the frequency matching command $S_1 = 1$, the rotor speed N_r is controlled to change f_r such that $f_r = f_m$. By the end of Stage-I (just before t_1), the frequency of $v_{r,a}$ is achieved equal to 49 Hz by regulating the VFT rotor speed at 0.5 p.u. (30 r/min) as per (17). Subsequent to successful completion of Stage-I at t_1, the status of commands S_1 and S_2 automatically

TABLE I
SYSTEM SPECIFICATIONS

WRIM specifications and parameters	
Power network-1	400 V, 50 Hz
Power network-1 series inductance	0.03 p.u.
Power network-II	392 V, 49 Hz
Power network-1I series inductance	0.052 p.u.
WRIM specifications and parameters	
Rated apparent power	4150 VA
Rated active power	3500 W
Rated voltage and frequency	400 V, 50 Hz
Number of poles	4
Stator to rotor turns ratio	400/400
Stator resistance	0.01965 p.u.
Stator inductance	0.0397 p.u.
Rotor resistance referred to stator	0.01965 p.u.
Rotor inductance referred to stator	0.0397 p.u.
Magnetizing (mutual) inductance	1.354 p.u.
Inertia constant	0.09526 s
DC motor drive specifications	
Rated output power	500 W
Rated armature voltage	500 V
Rated field voltage	300 V
Number of poles	4
Mechanical gear ratio	1/10
Electrical connection of dc drive	To power network-I

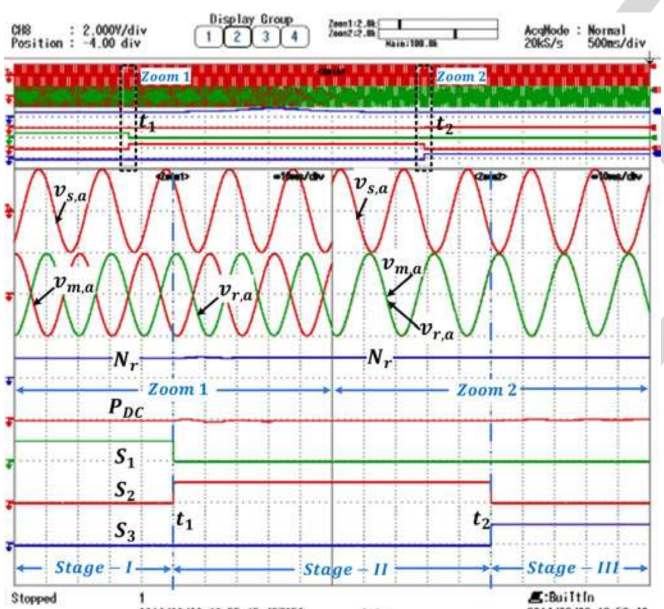

Fig. 7. Different stages in the proposed hierarchical control.

changes to $S_1 = 0$ and $S_2 = 1$ (Zoom1). In Stage-II, the phase angle matching of $v_{r,a}$ and $v_{m,a}$ is performed. To match the phase angles of both the voltages by changing the instantaneous rotor position of VFT, the speed of dc motor drive temporarily deviates from its reference speed. This operation can be seen from the temporary variations in N_r and the power handled by the dc drive ($P_{\rm dc}$). The successful matching of frequencies and phase angles of $v_{r,a}$ and $v_{m,a}$ can be observed from Zoom2 (just before time t_2). Stage-II ends at t_2 where the status of commands S_2 and S_3 are changed to $S_2 = 0$ and $S_1 = 1$ and

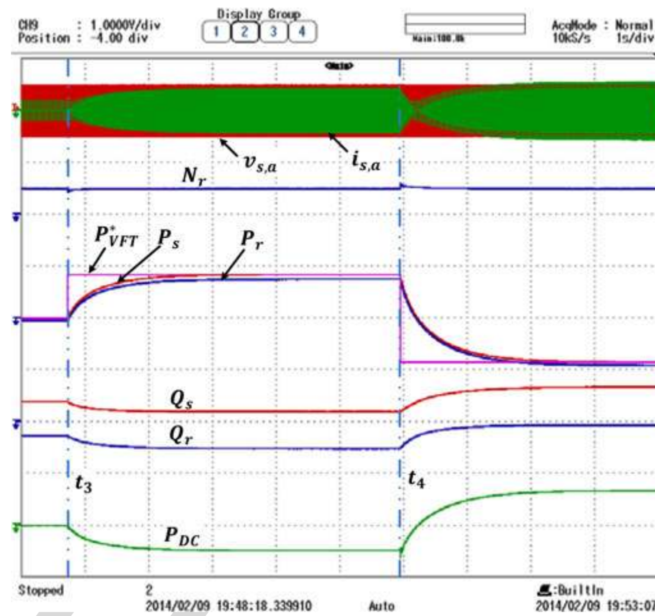

Fig. 8. Power control using the hierarchical control (dynamic performance).

the circuit breaker CB2 is closed to initiate the power transfer stage (Stage-III).

The performance of VFT during Stage-III is depicted in Figs. 8 and 9. According to power flow directions considered in Fig. 1, the positive value of $P^*_{\rm VFT}$ represents the power transferred from PN-I (stator side) to PN-II (rotor side) and negative quantity represents the reverse power flow.

The dynamic response of VFT during sudden changes in power transfer command ($P^*_{\rm VFT}$) is shown in Fig. 8. Initially, $P^*_{\rm VFT}$ is set equal to zero, and at t_3, it is changed from 0 to 0.85 p.u. It can be noticed that P_s and P_r reach the steady state ($P_s = P^*_{\rm VFT}$) within 3 s. Further to check the response of VFT during power reversal, $P^*_{\rm VFT}$ is changed from 0.85 to -0.85 p.u. at t_4. It can be observed that VFT reaches the new steady state within 3 s in this case as well. Note that, due to the active power loss in VFT there is a small difference between P_s and P_r during the steady state. The active power supplied/absorbed by the dc drive is governed by the direction of power transfer and it is observed around 0.5–0.7 p.u. (around 0.012–0.015 p.u. on VFT power base).

The expanded view of steady-state results for $P^*_{\rm VFT}$ equal to 0.85 and –0.85 p.u. is shown in Fig. 9 in Zoom1 and Zoom2, respectively. In Zoom1, it can be noticed that the stator current $i_{s,a}$ is nearly in-phase with stator voltage $v_{s,a}$ as the power is being transferred from PN-I to PN-II. Whereas in case of reverse power flow (Zoom2), $i_{s,a}$ is noticed to be almost out-of-phase with $v_{s,a}$. The change in Q_S and Q_r with the change in $P^*_{\rm VFT}$ (in Figs. 8 and 9) represents their uncontrolled nature as discussed in Section III-B. Due to this, the stator current ($i_{s,a}$) magnitudes are different for the same amount of active power flow in both directions. Note that the difference between Q_S and Q_r is almost constant as per (13) and is equal to the reactive power absorbed/required by VFT (Q_m).

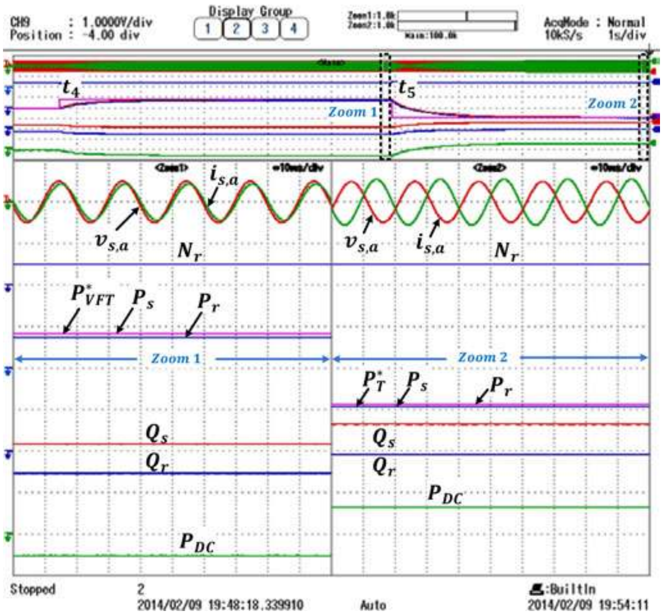

Fig. 9. Power control using the hierarchical control (steady-state performance).

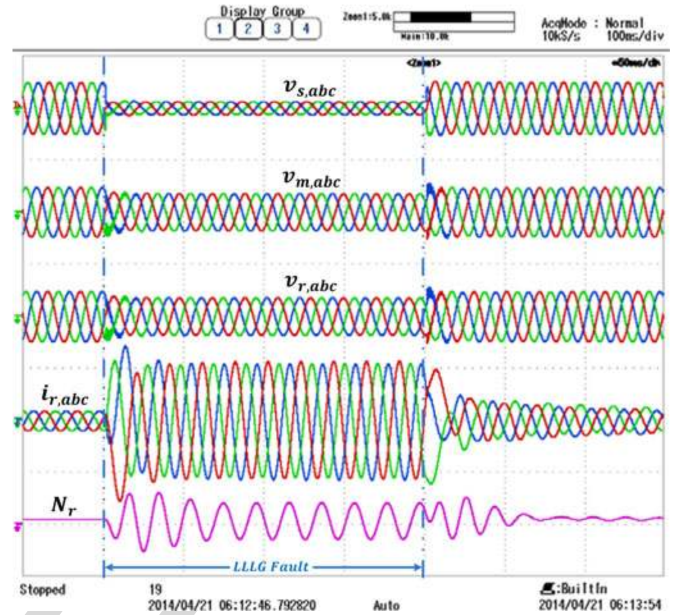

Fig. 11. VFT performance during three-phase fault in PN-I (stator side) without SDBR protection scheme.

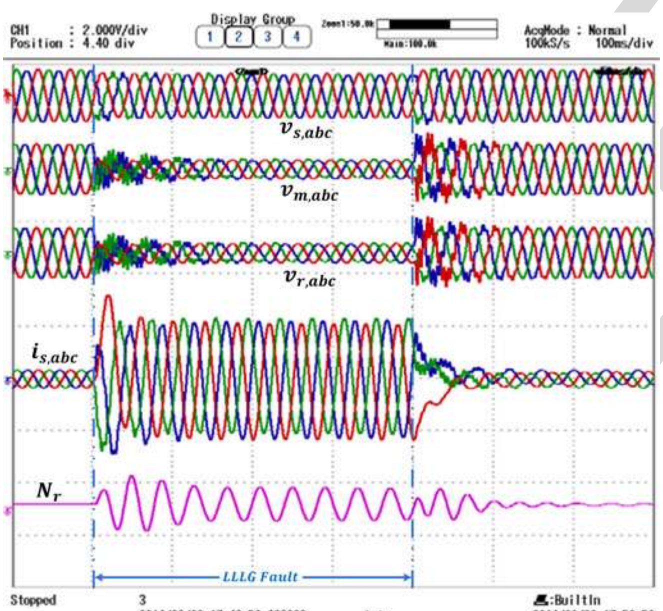

Fig. 10. VFT performance during three-phase fault in PN-II (rotor side) without SDBR protection scheme.

B. Fault Ride-Through Performance

The behavior of VFT without any additional FRT mechanism, during the three-phase grid fault at PN-II is shown in Fig. 10. The important variables that depict the fault propagation problem with VFT are shown in Fig. 10. These variables include: PN-I voltage at PCC-I ($v_{s,\mathrm{abc}}$: $1\ \mathrm{div} = 2$ p.u.), the PN-II voltage at PCC-II ($v_{m,\mathrm{abc}}$: $1\ \mathrm{div} = 2$ p.u.), the rotor voltage ($v_{r,\mathrm{abc}}$: $1\ \mathrm{div} = 2$ p.u.), current drawn from PN-I ($i_{s,\mathrm{abc}}$: $1\ \mathrm{div} = 5$ p.u.), and the rotor speed (N_r: $1\ \mathrm{div} = 5$ p.u.). Prior to the grid fault, the system is under steady state with a power transfer of 0.85 p.u. from PN-I to PN-II. A significant voltage dip in both PCC-II ($v_{m,\mathrm{abc}}$) and rotor ($v_{r,\mathrm{abc}}$) voltages and sudden rise in stator current ($i_{s,\mathrm{abc}}$) can be noticed during the grid fault condition. The rise in stator current signifies that the fault in the rotor side (PN-II) is propagated to the stator side (PN-I). The fault current in PN-I reaches 5 p.u. which may cause threat to PN-I security and reliability. Moreover, the large oscillations introduced in the rotor speed (N_r) during the grid fault causes the sustained mechanical vibrations that may destroy the WRIM and dc motor bearings.

The fault propagation from the stator side to rotor side during a grid fault on stator side (PN-I) is depicted in Fig. 11. It can be noticed that the rotor current rises 5 p.u. during the fault without SDBR protection. This signifies the fault propagation from PN-I to PN-II.

To avoid such high fault currents and mechanical stress due to fault propagation, the SDBR protection scheme shown in Fig. 4 is designed (explained in Section III). The set of specifications considered during the SDBR design are: $V_{\mathrm{fault\_min}} = 0.1$ pu, $V_{\mathrm{fault\_max}} = 0.9$ pu, $P_{\mathrm{rated}} = 0.85$ p.u, $k = 1.1$ and $V_{r\_\mathrm{min}} = 0.9$ pu. The values for $R_{\mathrm{SDBR\_max}}$ and $R_{\mathrm{SDBR\_min}}$ calculated using (14) and (15) are 4 Ω and 40 Ω, respectively. From (16), the SDBR resistance values computed are $R_1 = 4\ \Omega$, $R_2 = 12\ \Omega$, and $R_3 = 24\ \Omega$ respectively.

The performance of VFT with the proposed SDBR scheme during three-phase to ground fault on PN-II is shown in Fig. 12. Due to the activation of SDBR scheme during the three-phase fault, the rotor voltage ($v_{r,\mathrm{abc}}$) is restored to the nominal level and the stator current ($i_{s,\mathrm{abc}}$) is restricted to the maximum rated current. As the activation of SDBR does not allow the stator current to reach high value, it prevents the fault propagation through VFT. The oscillations in the speed are also reduced with

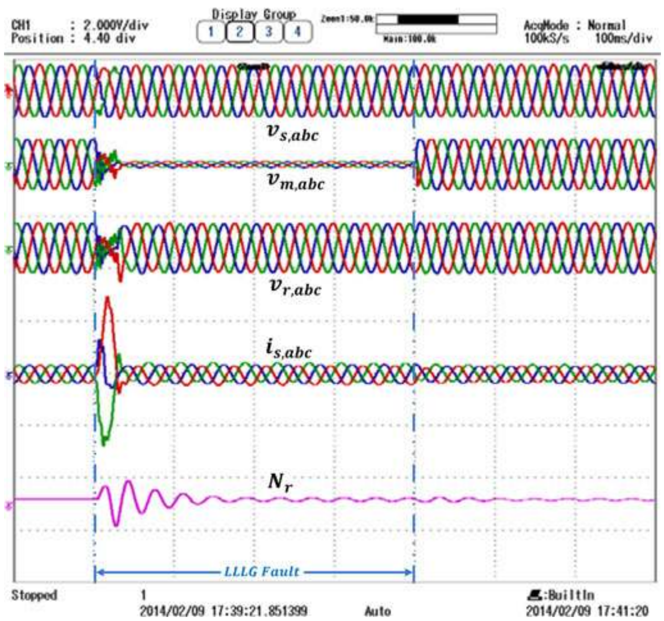

Fig. 12. VFT performance during three-phase fault in PN-II (rotor side) with the SDBR protection scheme.

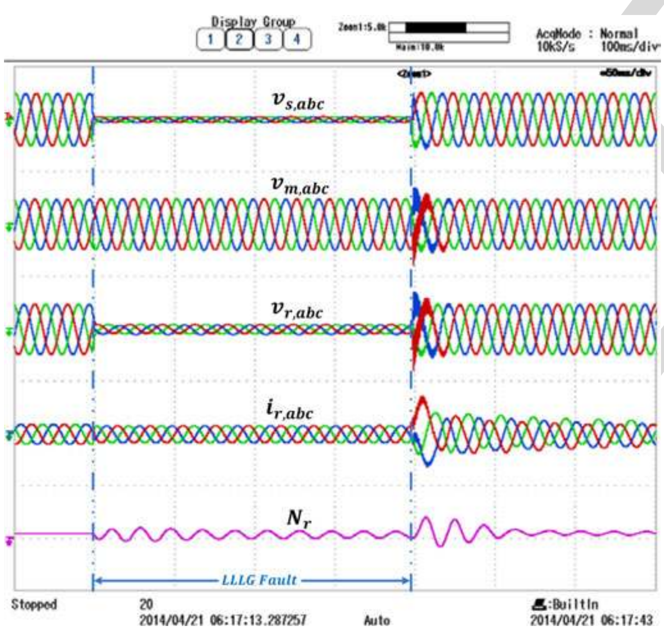

Fig. 13. VFT performance during three-phase fault in PN-I (stator side) with the SDBR protection scheme.

the SDBR and are damped out due to the presence of mechanical inertia and opposing torque produced by the dc motor drive.

The performance of VFT with the proposed SDBR protection scheme during the three-phase to ground fault on the stator side (PN-I) is depicted in Fig. 13. It can be observed that the grid fault on the stator side causes a sudden dip in stator voltage, $v_{s,\mathrm{abc}}$. During this condition, the insertion of SDBR series resistance on the rotor side brings down the $v_{r,\mathrm{abc}}$ without affecting $v_{m,\mathrm{abc}}$. This restricts the flow of fault current through VFT to a nominal level as noticed from $i_{r,\mathrm{abc}}$. Note that the rise in $i_{r,\mathrm{abc}}$ immediately after the fault clearance is mainly due to the sudden change in stator flux caused by the abrupt recovery of stator voltage.

The satisfactory performance during the steady-state, dynamic, and grid fault conditions proves that VFT with proposed SDBR scheme and hierarchical control strategy is a potential contender for the application of controlled power transfer between two asynchronous power networks.

VII. Conclusion

This paper presents a new hierarchical control strategy to control the VFT during normal and FRT operating conditions. This paper further investigates the possible fault propagation issue through VFT from one network to another. The SDBR-based FRT scheme has been proposed for VFT to mitigate the fault propagation. The detailed working principles of the VFT, all the stages of hierarchical control and FRT operation are verified using the real-time HIL system.

The detailed results under three stages of the proposed hierarchical control (frequency matching, phase angle matching, and power transfer control) during steady-state and dynamic conditions prove its comprehensiveness. The satisfactory results in limiting the fault propagation through VFT during the grid faults validate the effectiveness of SDBR protection scheme. In summary, along with the power transfer control function of VFT, added capability to limit the fault propagation and inherent natural damping capability will make VFT an ideal solution for the interconnection of micro grids in the future power systems.

References

[1] M. P. Bahrman, "Overview of HVDC transmission," in *Proc. Power Syst. Conf. Expo.*, 2006, pp. 18–23.
[2] A. Merkhouf, P. Doyon, and S. Uphadayay, "Variable frequency transformer—Concept and electromagnetic design evaluation," *IEEE Trans. Energy Convers.*, vol. 23, no. 4, pp. 989–996, Dec. 2008.
[3] E. Larsen, "A classical approach to constructing a power flow controller," in *Proc. IEEE Power Eng. Soc. Summer Meeting*, 1999, vol. 2, pp. 1192–1195.
[4] R. J. Piwko, E. V. Larsen, and C. A. Wegner, "Variable frequency transformer—a new alternative for asynchronous power transfer" in *Proc. IEEE Power Eng. Soc. Conf. Expo.*, Durban, Jul. 2005, pp. 393–398.
[5] B. Bagen, D. Jacobson, G. Lane, and H. M. Turanli, "Evaluation of the performance of back-to-back HVDC converter and variable frequency transformer for power flow control in a weak interconnection," presented at IEEE Power Eng. Soc. Gen. Meeting, Tampa, FL, USA , Jun. 24–28, 2007, pp. 1–6
[6] A. S. Abdel-Khalik, A. Elserougi, S. Ahmed, and A. Massoud, "Brushless doubly fed induction machine as a variable frequency transformer," in *Proc. 6th IET Int. Conf. Power Electron., Mach. Drives*, Mar. 2012. Q3
[7] A. H. El Din, M. A. Abdullah, and M. Ibrahim, "A Matlab/Simulink model to study the performance of the VFT for the interconnection of weak and strong AC grids," in *Proc. IEEE Int. Elect. Mach. Drives Conf.*, May 2011, pp. 1635–1640.
[8] E. T. Raslan, A. S. Abdel-Khalik, M. Abdulla, and M. Z. Mustafa, "Performance of VFT when connecting two power grids operating under different frequencies," in *Proc. 5th IET Int. Conf. Power Electron., Mach. Drives*, 19–21, Apr. 2010, pp. 1–6.
[9] G. Chen and X. Zhou, "Digital simulation of variable frequency transformers for asynchronous interconnection in power system," in *Proc. IEEE Power Eng. Soc. Transmiss. Distrib. Conf.*, 2005, pp. 1–6.

[10] L. Contreras-Aguilar and N. Garcia, "Accelerated time domain solution of VFT using the Poincaré map method with an embedded implicit integration algorithm" in *Proc. North Am. Power Symp.*, Calgary, Canada Sep. 2008, pp. 1–8.

[11] L. Contreras-Aguilar and N. Garcia, "Fast convergence to the steady state operating point of a VFT park using the limit cycle method and a reduced order model," in *Proc. IEEE Power Eng. Soc. Gen. Meeting*, Calgary, Canada, Jul. 2009, pp. 1–5.

[12] L. Contreras-Aguilar and N. Garcia, "Steady-state solution of a VFT park using the Newton method and a reduced order model," in *Proc. IEEE Power Tech.*, Bucharest, Rumania, Jun./Jul. 2009, pp. 1–6.

[13] L. Wang and L. Y. Chen, "Reduction of power fluctuations of a large scale grid-connected offshore wind farm using a variable frequency transformer," *IEEE Trans. Sustain. Energy*, vol. 2, no. 3, pp. 226–234, Jul. 2011.

[14] G. Poddar and V. T. Ranganathan, "Direct torque and frequency control of double-inverter-fed slip-ring induction motor drive," *IEEE Trans. Ind. Electron.*, vol. 51, no. 6, pp. 1329–1337, Dec. 2004.

[15] P. Marken, J. Roedel, D. Nadeau, D. Wallace, and H. Mongeau, "VFT maintenance and operating performance," in *Proc. Power Eng. Soc. Gen. Meeting Convers. Del. Elect. Energy*, Jul. 2008, pp. 1–5.

[16] D. Nadeau, "A 100-MW variable frequency transformer (VFT) on the Hydro-Quebec TransEnergie Network-the behavior during disturbance" in *Proc. Power Eng. Soc. Gen. Meeting*, Jun. 2007, pp. 1–5.

Bharath Babu Ambati received the B.E. degree in electrical and electronics engineering from the Sir C. R. Reddy College of Engineering (affiliated with Andhra University), Eluru, AP, India, in 2009; the M.Tech. degree in power electronics, electrical machines, and drives (PEEMD) from the Indian Institute of Technology (IIT) Delhi, New Delhi, India, in 2011; and is currently pursuing the Ph.D. degree in interdisciplinary engineering with the Masdar Institute of Science and Technology, Abu Dhabi, UAE.

From 2011 to 2012, he was with Schneider Electric India Private Limited as a Product Expert of Motion and Drives. His current research interests include power electronics, electrical machines, renewable energy generation, and power quality.

Parag Kanjiya received the B.Eng. degree in electrical engineering from the B.V.M. Engineering College, Sardar Patel University, V.V. Nagar, India, in 2009, and the M.Tech. degree in power systems from the Indian Institute of Technology Delhi (IITD), New Delhi, India, in 2011.

Since October 2011, he has been a Research Engineer with the Masdar Institute of Science and Technology, Abu Dhabi, UAE. His research interests include applications of power electronics in distribution systems, power quality enhancement, renewable energy, FACTS, and power system optimization.

Mr. Kanjiya was awarded the K.S. Prakasa Rao Memorial Award for earning the highest C.G.P.A at IITD in August, 2011.

Vinod Khadkikar (S'06–M'09) received the B.E. degree from the Government College of Engineering, Dr. Babasaheb Ambedkar Marathwada University, Aurangabad, India, in 2000; the M. Tech. degree from the Indian Institute of Technology (IITD), New Delhi, India, in 2002; and the Ph.D. degree from the École de Technologie Supérieure (ETS), Montréal, QC, Canada, in 2008, all in electrical engineering.

From December 2008 to March 2010, he was a Post-Doctoral Fellow at the University of Western Ontario, London, ON, Canada. From April 2010 to December 2010, he was visiting faculty at the Massachusetts Institute of Technology, Cambridge, MA, USA. Currently, he is an Associate Professor at the Masdar Institute of Science and Technology, Abu Dhabi, UAE. His research interests include applications of power electronics in distribution systems and renewable energy resources, grid interconnection issues, power quality enhancement, active power filters, and electric vehicles.

Dr. Khadkikar is currently an Associate Editor of the *IET Power Electronics Journal*.

Mohamed Shawky El Moursi (M'12) received the B.Sc. and M.Sc. degrees from Mansoura University, Mansoura, Egypt, in 1997 and 2002, respectively, and the Ph.D. degree from the University of New Brunswick (UNB), Fredericton, NB, Canada, in 2005, all in electrical engineering.

He was a Research and Teaching Assistant in the Department of Electrical and Computer Engineering, UNB, from 2002 to 2005. He joined McGill University as a Post-Doctoral Fellow with the Power Electronics Group. He joined Vestas Wind Systems, Arhus, Denmark, in the Technology R&D Group with the Wind Power Plant Group. He was with TRANSCO, UAE, as a Senior Study and Planning Engineer, and seconded as a Faculty Member in the Faculty of Engineering, Mansoura University. He was a Visiting Professor at the Massachusetts Institute of Technology, Cambridge, MA, USA. He is currently an Associate Professor in the Electrical Engineering and Computer Science Department, Masdar Institute of Science and Technology. His research interests include power system, power electronics, FACTS technologies, system control, wind turbine modeling, wind energy integration, and interconnections.

He is serving as an Associate Editor for *IET Renewable Power Generation* and *IET Power Electronics Journals*.

James L. Kirtley Jr. (F'91) received the Ph.D. degree from the Massachusetts Institute of Technology (MIT), Cambridge, MA, USA, in 1971.

He has been with the Large Steam Turbine Generator Department General Electric, and with Satcon Technology Corporation. Currently, he is a Professor of Electrical Engineering at MIT.

Dr. Kirtley served as an Editor-in-Chief of the IEEE TRANSACTIONS ON ENERGY CONVERSION from 1998 to 2006, and continues to serve as Editor and as a Member of the Editorial Board of *Electric Power Components and Systems*. He was awarded the IEEE Third Millennium Medal in 2000 and the Nikola Tesla Prize in 2002. He is a Registered Professional Engineer in Massachusetts and is a member of the United States National Academy of Engineering.

QUERIES

Q1. Author: Please spell out of OPAL-RT, PID, FACTS and C.G.P.A.
Q2. Author: Please check whether the edit in the sentence starting: “The dc motor drive power . . . .” is ok.
Q3. Author: Please provide page range in Ref. [6].
Q4. Author: Please provide location details.
Q5. Author: Please check if the edits to the BIOS of author “Vinod Khadkikar” are ok.
Q6. Author: Please provide location details.
Q7. Author: Please provide field of study.
Q8. Author: Please provide location details.

A Hierarchical Control Strategy With Fault Ride-Through Capability for Variable Frequency Transformer

Bharath Babu Ambati, Parag Kanjiya, Vinod Khadkikar, *Member, IEEE*, Mohamed Shawky El-Moursi*, Member, IEEE*, and James L. Kirtley Jr.*, Fellow, IEEE*

***Abstract*—A variable frequency transformer (VFT) is being considered as a new alternative to the classical back-to-back high voltage direct current (HVDC) system for interconnection of two asynchronous networks. The VFT is a retrospective form of frequency converter using the wound rotor induction machine (WRIM), which converts the constant frequency input into a variable frequency output. The prime objective of VFT is to achieve controlled bidirectional power transfer between the two asynchronous networks. This paper presents a detailed working principle of VFT technology and proposes a new hierarchical control strategy for establishing the VFT connection with two power systems to achieve bidirectional power transfer between them. Also, to restrict the grid fault propagation from one side of the VFT to the other side, a series dynamic braking resistor based fault ride-through (FRT) scheme is proposed. The performance of the VFT during synchronization process, steady-state, dynamic, and the grid fault conditions is evaluated using the real-time hardware in-loop (HIL) system. The plant is simulated in real time using OPAL-RT real-time simulator while the control algorithm is implemented in digital signal processor to carry out HIL study. All the important results supporting the effectiveness of the proposed control strategy and FRT scheme are discussed.**

***Index Terms*—Fault propagation, hierarchical control, power flow control, rotating transformer, series dynamic breaking resistor (SDBR), variable frequency transformer (VFT).**

I. Introduction

IN GENERAL, the interconnection of two different power networks with controlled power transfer capability can be achieved by a synchronous tie using a phase-shifting transformer or by an asynchronous tie using classical back-to-back high voltage direct current (HVDC) link. In the modern power systems, establishing a synchronous tie between two power networks would be a challenging task especially when one or both the networks experience a slight variation in their frequencies [1]. Moreover, the use of phase-shifting transformers in synchronous ties suffers from the drawbacks such as slow and step-wise controls [2]. This further causes wear and tear of tap changer contacts. Although, the use of power electronic controlled phase-shifting transformer can eliminate these drawbacks, they introduce additional problems such as harmonics, resonance, vulnerability to voltage surges, and reduced overloading capability due to their low thermal time constant [2], [3]. On the other hand, a back-to-back HVDC link can be established between any two power networks to achieve the controlled power flow between them. A line commutated converter (LCC)-based HVDC link suffers with the bottlenecks such as large reactive power requirements, lower thermal time constant, and lack of inertia for natural damping. Whereas, the voltage source converter (VSC)-based HVDC link can control the reactive power unlike LCC-based HVDC link. But, the inertia contribution and frequency response are still the challenges for HVDC technologies. Alternatively, the use of variable frequency transformer (VFT) for asynchronous interconnection can improve the system inertia and frequency control.

The VFT was first developed by General Electric Company in 2004 to achieve the interconnection of two different power networks [2]. A VFT is a controllable bidirectional power transfer device between the two asynchronous power networks that consists of wound rotor induction machine (WRIM) and a dc motor drive [2]. The presence of rotating mass (of both WRIM and dc motor) adds inertia to the power systems and thereby improves the stability during system disturbances. The VFT offers significant benefits over the widely installed LCC–HVDC link [4]–[6], mainly, lower reactive power requirements, harmonic-free power transfer, and higher system stability.

Basic concept and design aspects of 100 MW VFT is presented in [2]. The performance of VFT during steady-state, dynamic, and transient conditions is evaluated using simulation studies in [7]–[12]. In [13], the offshore wind park is connected to the grid through VFT to reduce the power fluctuations using the PID damping torque controller of the dc motor drive. Moreover, the use of brushless doubly fed induction machine (BDFIM) with squirrel cage rotor as alternative VFT configuration is reported in [6]. In which, the dual stator winding with different pole numbers with a ratio of 1:3 is used to avoid space harmonics concerns. The operating performance and maintenance of VFT is discussed in [15] and [16].

The steady-state analysis of the VFT is well established in the literature [2]–[12], but the problem of fault propagation and the fault ride-through (FRT) enhancement is not addressed so far. As

Manuscript received October 28, 2013; revised February 27, 2014 and May 19, 2014; accepted June 21, 2014. Paper no. TEC-00638-2013.

B. B. Ambati, P. Kanjiya, and V. Khadkikar are with the Center for Energy, Masdar Institute of Science and Technology, Abu Dhabi, 54224, UAE (e-mail: bambati@masdar.ac.ae; pkanjiya@masdar.ac.ae; vkhadkikar@masdar.ac.ae).

M. S. El-Moursi and J. L. Kirtley Jr. are with the Department of Electrical Engineering and Computer Science, Massachusetts Institute of Technology, Cambridge, MA 02139 USA. (e-mail: melmoursi@masdar.ac.ae; kirtley@mit.edu).

Color versions of one or more of the figures in this paper are available online at http:ieeexplore.ieee.org.

Digital Object Identifier 10.1109/TEC.2014.2336981

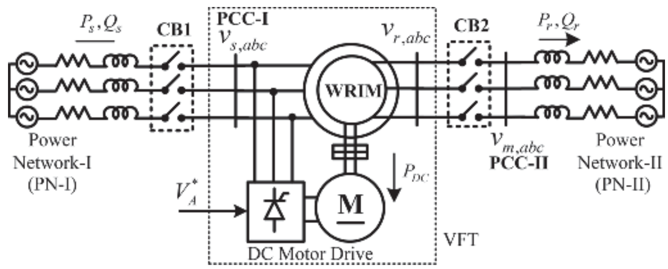

Fig. 1. VFT system configuration.

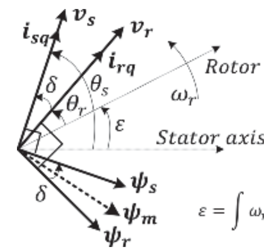

Fig. 2. Stator and rotor fluxes and voltages in VFT.

the fault propagation is a critical issue that affects power system reliability and security, the FRT protection schemes should be deployed in the VFT. In addition to that, the detailed control strategy for VFT is not presented in the literature.

This paper presents a detailed hierarchical control strategy for the VFT to achieve the following functions: establish a connection between two power systems, power transfer control, and FRT operation. Furthermore, a new topology of VFT comprising a series dynamic braking resistor (SDBR) is proposed to enhance the FRT capability. A number of states are defined for VFT operation to effectively connect it, operate it in steady state, and protect it during the grid faults. The proposed control strategy and VFT configuration are validated using real-time hardware in-loop (HIL) simulation. The plant is simulated in real time using OPAL-RT real-time simulator while the control algorithm is implemented in dSPACE-1103 to carry out HIL study.

II. Variable Frequency Transformer

Fig. 1 shows the VFT system configuration that consists of a WRIM mechanically coupled with a dc motor drive. The three-phase stator and rotor windings of WRIM are connected to two asynchronous power networks namely power network-I (PN-I) and power network-II (PN-II) as illustrated in Fig. 1. The frequencies and/or phase angles of both PN-I (f_s and θ_s) and PN-II (f_m and θ_m) could be different in actual application.

To connect the stationary VFT to the PN-I and PN-II simultaneously, the frequencies (f_s and f_m) and phase angles (θ_s and θ_m) should be identical. It is difficult to achieve this condition in practical system. Therefore, the following approach is deployed with the VFT to make this asynchronous interconnection.

1) Connect the PN-I directly to the stator side of the VFT (by closing CB1) while keeping the rotor stationary and circuit breaker CB2 open.
2) Measure the frequency f_r and phase angle θ_r of the voltage induced in the rotor windings ($v_{r,\mathrm{abc}}$) at the terminals of CB2 (when the rotor is stationary, $f_r = f_s$ and $\theta_r = \theta_s$).
3) Measure the frequency f_m and phase angle θ_m of PN-II voltage ($v_{m,\mathrm{abc}}$) available on the other side of CB2.
4) Control the rotor speed to change f_r by using the dc motor drive to achieve $f_r = f_m$.
5) Adjust the rotor position (θ_r) using the dc motor drive to make $\theta_r = \theta_m$.
6) The synchronization between voltages $v_{r,\mathrm{abc}}$ and $v_{m,\mathrm{abc}}$ is achieved by steps 4 and 5, then the CB2 can be closed to establish the interconnection between both networks through VFT.

Here onwards, the points 4 and 5 are referred as frequency matching and phase angle matching, respectively. A control algorithm required to control the dc motor drive in VFT is developed in Section V.

III. VFT Concept and Power Flow

Based on the existing literature, the working principle and the active and reactive power flow through the VFT have not been discussed in detail. In addition to that, FRT operation and protection strategy have not been addressed. Hence, the detailed VFT model is developed to study all the operational aspects for steady-state, dynamic, and transient conditions.

A. Active Power Transfer and Control

The synchronization procedure described in the previous section is used to connect both power networks in Fig. 1. Consequently, both the stator and rotor fluxes will be in synchronism irrespective of the rotor speed with a specific phase angle difference represented as load angle (δ). The controllability of this load angle δ and its effect on active power transfer between both networks is analyzed in this subsection.

The stator and rotor voltage vectors and the respective flux vectors referred to stator are shown in Fig. 2. The instantaneous stator flux ($\boldsymbol{\psi}_\mathbf{s}$), air-gap flux ($\boldsymbol{\psi}_\mathbf{m}$) and rotor flux ($\boldsymbol{\psi}_\mathbf{r}$) vectors in the stationary reference frame can be expressed as

$$\boldsymbol{\psi}_\mathbf{s} = L_s \mathbf{i}_\mathbf{s} + L_m \left(\mathbf{i}_\mathbf{r} \mathbf{e}^{\mathrm{j}\varepsilon}\right) \quad (1)$$

$$\boldsymbol{\psi}_\mathbf{m} = L_m \left(\mathbf{i}_\mathbf{s} + \left(\mathbf{i}_\mathbf{r} \mathbf{e}^{\mathrm{j}\varepsilon}\right)\right) \quad (2)$$

$$\boldsymbol{\psi}_\mathbf{r} = L_r \mathbf{i}_\mathbf{r} + L_m \left(\mathbf{i}_\mathbf{s} \mathbf{e}^{-\mathrm{j}\varepsilon}\right) \quad (3)$$

where L_s, L_r, and L_m represent the equivalent stator, rotor, and mutual inductances referred to stator side; $\mathbf{i}_\mathbf{s}$ and $\mathbf{i}_\mathbf{r}$ are the stator and rotor currents, respectively. ε is the angular displacement between the stator and rotor fluxes and ω_r is the angular (mechanical) speed of the rotor.

From Fig. 2 and (1)–(3), the expression for the electromagnetic torque (T_e) can be obtained as [14]

$$T_e = \frac{2}{3}\frac{p}{2}\frac{L_m}{L_s L_r}\mathrm{Im}\left[\boldsymbol{\psi}_\mathbf{s}\boldsymbol{\psi}_\mathbf{r}^*\right] = \frac{2}{3}\frac{p}{2}\frac{L_m}{L_s L_r}\left|\boldsymbol{\psi}_\mathbf{s}\right|\left|\boldsymbol{\psi}_\mathbf{r}^*\right|\sin\delta. \quad (4)$$

The aforementioned relationship shows that the electromagnetic torque developed is a cross product of stator and rotor fluxes, i.e., the product of magnitudes of $\boldsymbol{\psi}_{\mathbf{s}}$, $\boldsymbol{\psi}_{\mathbf{r}}$, and the sine of the angle δ between both the fluxes. On the other hand, general expression for the developed electromagnetic torque in any reference frame (*d*–*q* or $\propto$–β) can be written as

$$T_e = k\boldsymbol{\psi}_{\mathbf{m}} i_q \tag{5}$$

where k is the torque constant, and i_q is component of current vector in quadrature with $\boldsymbol{\psi}_{\mathbf{m}}$. Here, the quadrature component of current refers to stator/rotor current as the angle between $\boldsymbol{\psi}_{\mathbf{m}}$ and $\boldsymbol{\psi}_{\mathbf{s}}$ or $\boldsymbol{\psi}_{\mathbf{m}}$ and $\boldsymbol{\psi}_{\mathbf{r}}$ is very small.

From the basic integral relation between the flux and voltage, a current that is in quadrature with the flux is in-phase or out-of-phase with the voltage and hence responsible for active power flow. In general, the VFT is connected between the two power systems whose voltages are fairly constant and hence the magnitudes of $\boldsymbol{\psi}_{\mathbf{s}}$, $\boldsymbol{\psi}_{\mathbf{r}}$, and $\boldsymbol{\psi}_{\mathbf{m}}$ can be treated as constants. Therefore, from (4) and (5) it can be deduced that the torque developed/imposed on the rotor is proportional to $'\mathrm{Sin}\,\delta'$ and active component of stator/rotor current. If the displacement angle ε in Fig. 2 is changed by applying external torque through the dc motor drive, the angle δ and hence electromagnetic torque developed in the WRIM will change according to (4). Consequently, it changes the active current (i_q) as per (5). It can be observed that the active current variation is in proportion to δ (as the δ is very small, $\mathrm{Sin}\,\delta \approx \delta$), which is analogous to a series inductor behavior. The generalized active power flow through the series inductor is expressed by

$$P = \frac{V_s V_r}{X_s} \sin \delta. \tag{6}$$

Therefore, for the case of VFT, considering a stator to rotor turns ratio of 1:1, and neglecting the losses in the system, the active power transfer (P_{VFT}) in terms of the stator and rotor voltages, from Fig. 2, can be written as

$$P_{\mathrm{VFT}} = \frac{V_s V_r}{X_s} \sin\left(\theta_s - (\theta_r + \varepsilon)\right) \tag{7}$$

where V_s and θ_s are the *rms* stator voltage and its phase angle, respectively; V_r and θ_r are the *rms* rotor voltage and its phase angle, respectively; and X_s is the series equivalent inductive reactance offered by the VFT. The term ε in (7) is the time integral of ω_r to be controlled by the dc motor drive.

By neglecting the leakage reactance and magnetizing current (i.e., power factors close to unity) of the VFT [2], the mechanical power handled by the dc motor drive can be expressed as

$$P_{\mathrm{dc}} = P_s - P_r = V_s I_s - V_r I_r \tag{8}$$

where I_s and I_r are the *rms* values of the active component of stator and rotor currents, respectively. Considering volt/hertz/turn and MMF balance between the stator and rotor windings of the VFT, the above expression can be rewritten as [2]

$$P_{\mathrm{dc}} = V_s I_s - \left(\frac{V_s}{N_s f_s} N_r f_r\right)\left(\frac{I_s N_s}{N_r}\right) = V_s I_s \left(1 - \frac{f_r}{f_s}\right) \tag{9}$$

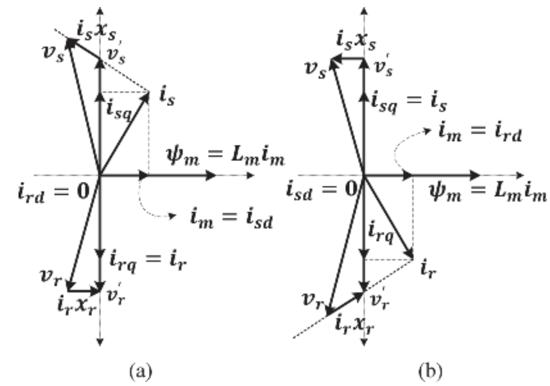

Fig. 3. Reactive power flow concept in the VFT. (a) $\nu_s > \nu_r$ (b) $\nu_s < \nu_r$

where N_s and N_r are the number of turns in the stator and rotor windings of VFT, respectively. From (9), it is clear that the power absorbed by the dc motor drive is a function of frequency difference between both the power networks and the power being transferred through the VFT. Also, from (9), the torque expression for the dc motor can be written as

$$T_{\mathrm{dc}} = \frac{P_{\mathrm{dc}}}{\omega_r} = \frac{V_S I_S \left(1 - \frac{f_r}{f_s}\right)}{2\pi \frac{120\,(f_s - f_r)/p}{60}} = \frac{p}{2}\frac{V_S I_S}{2\pi f_s} \tag{10}$$

where p is number of poles in the WRIM. From (10), it can be noticed that the torque developed by the dc motor drive is independent of speed of rotation. Assuming the constant stator voltage in (10), it can be noticed that by changing the torque applied through dc motor drive, the stator active current (I_S) can be changed. This proves the correlation between torque applied by dc motor drive and active current transferred through VFT according to (5). A simple armature voltage controlled four quadrant dc drive can be employed to regulate the torque produced by the dc motor and thereby active power transfer.

B. Reactive Power Transfer

Stator and rotor reactive currents (i_{sd} and i_{rd}) of VFT may consists of two components: 1) the magnetizing current required for VFT operation (i_m); and 2) the reactive current transferred between the two networks. The amount of reactive current supplied/absorbed by each network is dependent on the voltage magnitudes at the stator (PCC-I) and rotor (PCC-II) terminals. Regardless of slight difference in grid voltages on both sides, the VFT maintains the volt/hertz/turn balance between induced stator (v_s') and rotor (v_r') voltages by circulating the appropriate amount of reactive current between both the networks.

Two different cases are demonstrated to show the reactive power flow dependency on the voltage magnitudes on both sides of VFT as illustrated in Fig. 3. The stator and rotor resistances are neglected and it is assumed that the active current transferred between the stator and rotor is constant ($i_{\mathrm{sq}} = -i_{\mathrm{rq}}$) throughout the operation. Fig. 3(a) represents the case where the stator voltage is slightly higher than the rotor voltage referred to stator side (i.e., $v_s > v_r$). Assuming the induced stator voltage (v_s')

is constant, any increase in v_s causes increase in i_s according to $v_s = v_s' + i_s x_s$. For the fixed active power transfer, active current (i_{sq}) is constant and hence reactive current (i_{sd}) has to increase in order to accommodate the change in i_s. In Fig. 3(a), the stator voltage magnitude is considered such that whole magnetizing current (i_m) required for VFT operation comes from the stator (i.e., $i_m = i_{\mathrm{sd}}$ and $i_{\mathrm{rd}} = 0$). Thus, further increase in the stator voltage magnitude leads to i_{sd} higher than i_m, that makes $i_{\mathrm{rd}} = -(i_{\mathrm{sd}} - i_m)$ which is the net reactive current transferred from PN-I to PN-II through VFT. Accordingly, any reduction in stator voltage magnitude drives the stator and rotor sides to supply the required magnetizing current i_m for VFT operation.

The vector diagram corresponding to the case where full magnetizing current is drawn from the rotor side due to higher rotor voltage is shown in Fig. 3(b). Similar to the aforementioned case, any further increase in the rotor voltage in Fig. 3(b) leads to reactive power flow from PN-II to PN-I.

It is obvious that the reactive power flow into/through VFT is uncontrolled and is mostly dependent on the terminal voltage magnitudes of v_s and v_r. The VFT requires a fixed amount of reactive power to meet the constant magnetization demand regardless of the amount and/or direction of active power transfer. The stator and rotor currents through VFT can be obtained from the steady-state equivalent circuit for particular voltage conditions and reactive powers can be computed as

$$Q_s = |\boldsymbol{\nu}_s|\,|\mathbf{i}_{\mathrm{sd}}| = \mathrm{Im}\,[\boldsymbol{\nu}_s i_s^*] \tag{11}$$

$$Q_r = |\boldsymbol{\nu}_r|\,|\mathbf{i}_{\mathrm{rd}}| = \mathrm{Im}\,[\boldsymbol{\nu}_r i_r^*]\,. \tag{12}$$

For the power flow directions shown in Fig. 1, the reactive power absorbed by VFT (Q_m) at any operating condition is the difference between stator and rotor reactive powers, i.e.,

$$Q_m = Q_s - Q_r. \tag{13}$$

IV. SDBR Protection Scheme for VFT

As discussed in the previous section, during the steady-state operation, VFT is analogous to a series inductor. Therefore, during a voltage dip resulted from the grid fault in one of the power networks, the other network is forced to supply a large fault currents. This indicates the propagation of a fault from the faulted network to the healthy power network through VFT. This fault propagation phenomenon associated with VFT has not been discussed in the literature. To demonstrate the problems associated with the fault propagation, a fault condition is considered at PN-II as shown in Fig. 1. This grid fault (or voltage dip) has the following consequences unless appropriate protective measures are taken:

1) large fault currents from the stator side;
2) temporary disconnection of VFT due to CB1 opening;
3) oscillations/instability in PN-I due to system dynamics;
4) slow post fault recovery due to VFT disconnection;
5) possible requirement of VFT resynchronization;
6) damage to VFT windings in the event of protection failure.

This paper introduces an appropriate FRT scheme within the VFT system using SDBR to overcome the issue of fault propagation as shown in Fig. 4. The SDBR protection scheme is identified as simple and economic solution for enhancing the FRT capability and transient performance of VFT in response to symmetrical and asymmetrical grid faults. It can be noted that, four different combinations of power flow direction (PN-I to PN-II or PN-II to PN-I) and the grid fault (in PN-I or PN-II) are possible in the VFT. The SDBR scheme that can prevent the fault propagation in all four possible cases can be designed using a simple approach by considering a power flow from PN-I to PN-II and the grid fault in PN-II as described in the following.

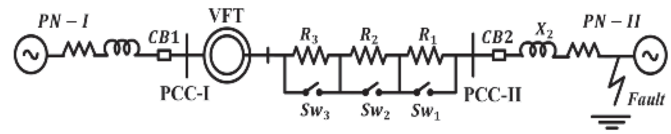

Fig. 4. Single line diagram of SDBR protection scheme for VFT.

A. Series Resistance Selection

According to the design criteria, the SDBR should limit the fault current by acting as a voltage booster against the voltage in PN-II at the rotor terminals and protect the healthy network (PN-I) connected to the stator terminal. To be able to work with various levels of grid faults (based on magnitudes of voltage dip), the SDBR should have different combination of resistors. The SDBR with n resistors can realize $(2^n - 1)$ combinations of resistances. The maximum and minimum possible resistance values of SDBR should be selected based on the following two scenarios.

1) Voltage Dip Operation: During the most severe grid fault, the voltage appears on the rotor terminals should be higher than the minimum allowable rotor voltage (V_{r_min}). The maximum value of series resistance ($R_{\mathrm{SDBR\_max}} = R_1 + R_2 + \ldots + R_n$) required to achieve this during the worst case voltage dip can be calculated using the following:

$$V_{\mathrm{fault\_min}} + \frac{P_{\mathrm{rated}}}{3V_{r\_\mathrm{min}}} R_{\mathrm{SDBR\_max}} \geq kV_{r\_\mathrm{min}} \tag{14}$$

where $V_{\mathrm{fault\_min}}$ is the lowest possible grid voltage (at PCC-II) during the grid fault on PN-II, P_{rated} is the rated power transfer capability of VFT, and k is safety margin (>1) to take care of the lagging power factor.

2) Overvoltage Protection: The designed SDBR should not cause the overvoltage across the rotor terminals in any case such as small voltage dips. The minimum value of series resistance ($R_{\mathrm{SDBR\_min}}$) that prevents the rotor overvoltage can be computed from the following equation:

$$V_{\mathrm{fault\_max}} + \frac{P_{\mathrm{rated}}}{3V_{r\_\mathrm{rated}}} R_{\mathrm{SDBR\_min}} \leq 3V_{r\_\mathrm{rated}} \tag{15}$$

where $V_{\mathrm{fault\_max}}$ is the grid voltage (at PCC-II) during the minor voltage dip that can trigger the SDBR. For the present case of SDBR with three resistances, the value of different resistors can be calculated from the maximum and minimum values of

SDBR resistances obtained through (14) and (15) as follows:

$$R_1 = R_{\mathrm{SDBR\_min}}$$
$$R_2 = \frac{1}{3}\left[R_{\mathrm{SDBR\_max}} - R_{\mathrm{SDBR\_min}}\right] \quad (16)$$
$$R_3 = \frac{2}{3}\left[R_{\mathrm{SDBR\_max}} - R_{\mathrm{SDBR\_min}}\right].$$

B. Static AC Switch Selection

Three SDBR resistors can be inserted into the circuit by controlling the static ac switches Sw_1, Sw_2, and Sw_3, respectively. Three ac switches are required for switching the resistors (R_1, R_2, and R_3) in each phase as per Fig. 4. Therefore, a total of nine resistors (R_1, R_2, and R_3 for each phase) and nine ac switches are deployed to realize the SDBR protection scheme.

The current rating of ac switches in SDBR scheme should be equal to the rated VFT current as they remain closed during the steady-state operation. And, the voltage rating of the switches should be equal to the product of rated VFT current and corresponding resistor value. It is worthy to note that the switching losses are absent (as switches are always closed) during the steady-state operation and therefore, the switches with low conduction losses are preferred for this SDBR scheme.

The ac switches can be realized using either antiparallel thyristors (low cost) or antiseries IGBTs (high cost). The choice of the switch depends on the speed requirement of resistor insertion during the fault. The antiparallel thyristor switch has a maximum of half cycle delay in operation as it breaks the current at next zero crossing while, antiseries IGBT switch can break the current instantaneously.

The WRIM in the VFT system possesses large thermal time constant and can easily handle the current surge resulted from the delay in ac switch opening. Therefore, the low cost antiparallel thyristor switches are used as ac switches in SDBR protection scheme.

V. Proposed Hierarchical Control Strategy

This section describes the overall control of VFT and SDBR. The dc motor drive is the only controllable device in a VFT system that can regulate the power flow between two power networks. However, as highlighted in the previous section SDBR is an additional controllable device for the restriction of fault propagation. A comprehensive hierarchical strategy, with all the necessary controls, is proposed in three operational stages.

When the stator is directly connected to PN-I and circuit breaker CB2 is open, the dc motor drive is to be controlled to achieve the frequency matching ($f_r = f_m$) and phase angle matching ($\theta_r = \theta_m$). This part of control is realized in first two stages (Stage-I and Stage-II) of the proposed hierarchical control. Once the connection is established between both the power networks through VFT, the power transfer control is carried out in Stage-III.

The control block diagram depicting these three stages of the proposed hierarchical control is shown in Fig. 5. A four-quadrant armature voltage control method is employed for dc drive in the proposed hierarchical control. The changeover from one stage to another is realized using the states S_1, S_2, and S_3 as illustrated in Fig. 5 with the predefined hierarchy depicted in Fig. 6. The control of SDBR protection scheme is also incorporated in the flow chart of Fig. 6. The objective and control of VFT in each stage of hierarchical control is discussed in the following subsections.

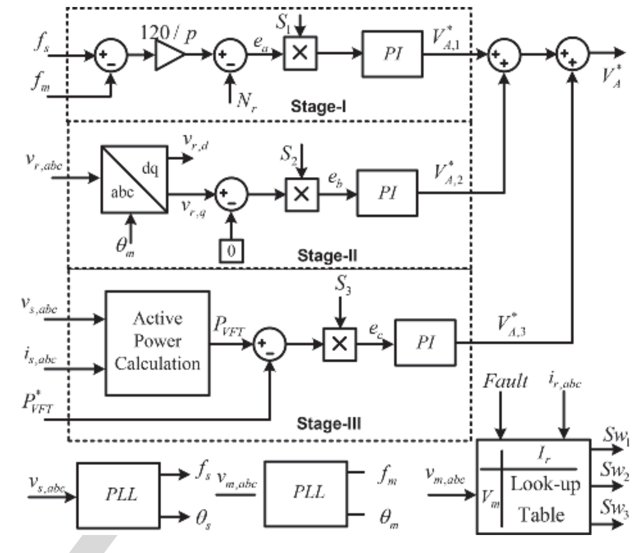

Fig. 5. Proposed hierarchical control strategy for synchronization and power transfer control in VFT.

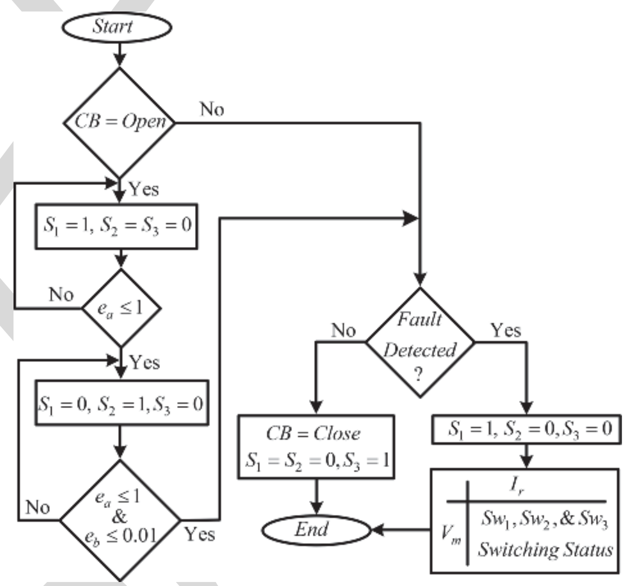

Fig. 6. Flow chart for hierarchical control strategy and SDBR control.

A. Stage-I: Frequency Matching

Initially when the stator of WRIM is connected to PN-I, the rotor is stationary and CB2 is open, the command $S_1 = 1$ is issued to start the frequency matching stage. At this condition the frequency of rotor voltage f_r has to be changed from $f_r = f_s$ to $f_r = f_m$. To achieve this desired frequency change, the equivalent rotor speed at which the rotor of VFT should be driven by dc motor drive is

$$N_r^* = \frac{120\,(f_s - f_m)}{p}. \tag{17}$$

The reference (N_r^*) and actual (N_r) speeds are compared, and the error, e_a, is processed through the PI controller to generate the necessary armature voltage ($V_{A,1}^*$) for the armature controlled dc motor drive (shown in Stage-I of Fig. 5). Once, the mean of absolute speed error (e_a) goes below 1 r/min, S_1 becomes low and S_2 becomes high as shown in the flow chart given in Fig. 6. Thereafter, high state of S_2 enables the next stage of hierarchical control.

B. Stage-II: Phase Angle Matching

Subsequent to the frequency matching, the next objective is to achieve the phase angle matching between $v_{r,\mathrm{abc}}$ and $v_{m,\mathrm{abc}}$ (i.e., $\theta_r = \theta_m$). Applying *abc–dq* transformation on the measured rotor voltages ($v_{r,\mathrm{abc}}$) using the phase angle (θ_m) of PN-II voltage ($v_{m,\mathrm{abc}}$), obtained from the phase locked loop (PLL), gives the direct ($v_{r,d}$) and quadrature ($v_{r,q}$) components of rotor voltages referred to PN-II voltage phasor. When the rotor voltage phase angle (θ_r) is exactly equal to θ_m, the computed $v_{r,q}$ becomes zero. In other words, by making $v_{r,q} = 0$, the phase angles can be matched (θ_r and θ_m). To achieve this, a PI controller is used over the $v_{r,q}$ for generating the necessary armature voltage ($V_{A,2}^*$) to change the rotor position (shown in Stage-II of Fig. 5). As soon as the mean of the absolute phase angle error (e_b or $v_{r,q}$) goes below certain margin (say 1%), S_2 goes low indicating the completion of Stage-II (shown in Fig. 6).

After frequency and phase angle matching are completed, the CB2 closes to establish the connection between both the networks through VFT. Subsequently, S_3 goes high to enable the power transfer controller.

C. Stage-III: Power Transfer Control

Actual power transfer (P_{VFT}) from PN-I to PN-II is measured on the stator side of VFT and compared with the reference power (P_{VFT}^*). The error is passed through the PI controller to generate the necessary armature voltage ($V_{A,3}^*$) and thus to control the torque developed by the dc motor drive (T_{dc}). The torque produced by dc motor drive dynamically adjusts the angle ε to achieve the desired load angle δ that makes $P_{\mathrm{VFT}}^* = P_{\mathrm{VFT}}$ as per (7).

The reference armature voltage (V_A^*) for the dc motor drive is expressed as follows:

$$V_A^* = V_{A,1}^* + V_{A,2}^* + V_{A,3}^*. \tag{18}$$

During the power transfer control, any change in the networks frequencies forces the rotor to adjust its speed according to (17).

D. SDBR-Based Fault Ride-Through Control

The SDBR control and fault detection is integrated in the hierarchical control strategy as shown in Fig. 6. When the grid fault occurs, the power transfer control should saturate at its prefault value to avoid rotor acceleration in response to fault conditions. This is achieved by forcing $S_3 = 0$ to keep the corresponding PI controller output at its prefault value. Whereas, the command $S_1 = 1$ (frequency matching loop) is reissued during the fault to damp out the rotor oscillations by controlling the torque of the dc motor drive. Simultaneously, there is a need to insert a suitable combination of resistors in SDBR that prevent the fault propagation from the faulted network to the healthy network. This is obtained using a two-dimensional (2 D) lookup table based on VFT current and fault voltage magnitudes. The output of lookup table is status of switches Sw_1, Sw_2, and Sw_3 that inserts a appropriate combination of R_1, R_2, and R_3. The switches Sw_1, Sw_2, and Sw_3 of each phase are simultaneously controlled for balanced faults while they are controlled independently for each phase during the unbalance faults. After the fault is cleared, the power transfer controller is reactivated to maintain the power transfer control by giving the control signals $S_1 = S_2 = 0, S_3 = 1$. The coordination between the three stages of the proposed hierarchical control and the proposed SDBR control is shown in Fig. 6.

VI. Real-Time Hardware In-Loop Validation

The proposed hierarchical control strategy and SDBR scheme for VFT are verified using a real-time HIL implementation. The control algorithm is implemented in the digital signal processor (DSP) board, DS1103 from dSPACE at a step size of 50 μs. The plant (VFT test system and SDBR scheme) is emulated using the OPAL-RT real-time simulator. The communication between the controller and the plant is carried out through ADC and DAC ports of DS1103 and OPAL-RT.

Due to high torque requirement by the VFT system during low speed operations, a geared dc motor with a mechanical gear of ratio 1:10 is used instead of conventional dc motor. The use of geared dc motors can significantly reduce the size of the dc motor during the actual applications of VFT. The system specifications and the machine parameters of VFT test system are given in Table I.

A. Steady-State Performance

The performance of VFT system during the three stages of proposed hierarchical control is shown in Figs. 7–9. All the results are given in per unit values with $1\ \mathrm{div} = 1$ p.u. The dc motor drive power P_{dc} and speed N_r are represented on the basis of 100 W and 60 r/min for a better visualization of their dynamics. The PN-I operates at 400 V/50 Hz while the PN-II operates at 392 V/49 Hz. The effectiveness of each stage of hierarchical control and the transition from one stage to another can be seen from Fig. 7. When VFT is stationary the frequency f_r of the induced rotor voltage ($v_{r,a}$) is 50 Hz while the frequency f_m of PN-II voltage ($v_{m,a}$) is 49 Hz. As highlighted in Section II, to close the circuit breaker CB2, synchronization should be established between the $v_{r,a}$ and $v_{m,a}$. Therefore in Stage-I, with the frequency matching command $S_1 = 1$, the rotor speed N_r is controlled to change f_r such that $f_r = f_m$. By the end of Stage-I (just before t_1), the frequency of $v_{r,a}$ is achieved equal to 49 Hz by regulating the VFT rotor speed at 0.5 p.u. (30 r/min) as per (17). Subsequent to successful completion of Stage-I at t_1, the status of commands S_1 and S_2 automatically

TABLE I
SYSTEM SPECIFICATIONS

WRIM specifications and parameters	
Power network-1	400 V, 50 Hz
Power network-1 series inductance	0.03 p.u.
Power network-II	392 V, 49 Hz
Power network-1I series inductance	0.052 p.u.
WRIM specifications and parameters	
Rated apparent power	4150 VA
Rated active power	3500 W
Rated voltage and frequency	400 V, 50 Hz
Number of poles	4
Stator to rotor turns ratio	400/400
Stator resistance	0.01965 p.u.
Stator inductance	0.0397 p.u.
Rotor resistance referred to stator	0.01965 p.u.
Rotor inductance referred to stator	0.0397 p.u.
Magnetizing (mutual) inductance	1.354 p.u.
Inertia constant	0.09526 s
DC motor drive specifications	
Rated output power	500 W
Rated armature voltage	500 V
Rated field voltage	300 V
Number of poles	4
Mechanical gear ratio	1/10
Electrical connection of dc drive	To power network-I

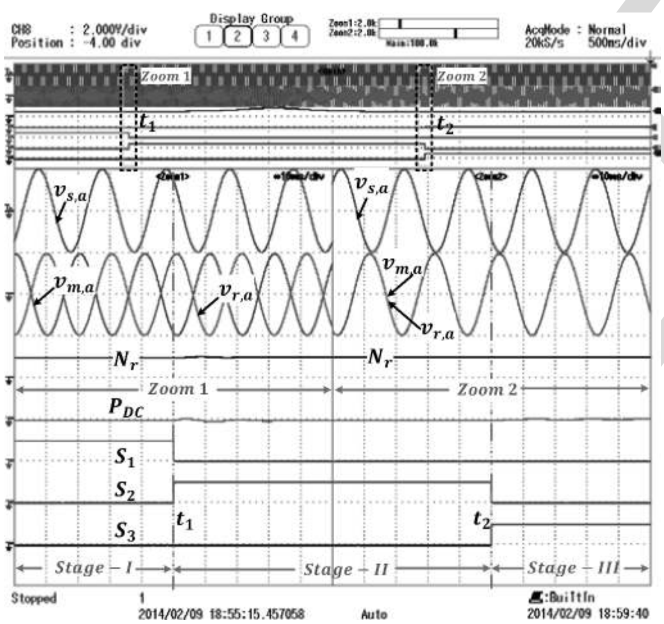

Fig. 7. Different stages in the proposed hierarchical control.

changes to $S_1 = 0$ and $S_2 = 1$ (Zoom1). In Stage-II, the phase angle matching of $v_{r,a}$ and $v_{m,a}$ is performed. To match the phase angles of both the voltages by changing the instantaneous rotor position of VFT, the speed of dc motor drive temporarily deviates from its reference speed. This operation can be seen from the temporary variations in N_r and the power handled by the dc drive ($P_{\rm dc}$). The successful matching of frequencies and phase angles of $v_{r,a}$ and $v_{m,a}$ can be observed from Zoom2 (just before time t_2). Stage-II ends at t_2 where the status of commands S_2 and S_3 are changed to $S_2 = 0$ and $S_1 = 1$ and

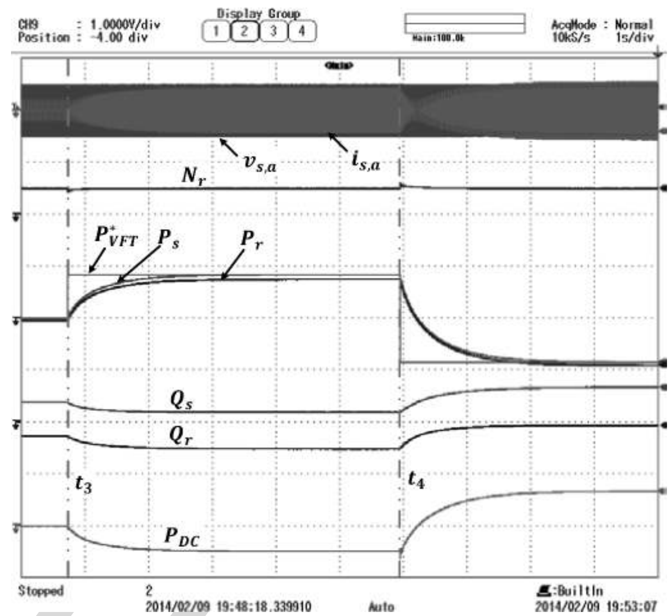

Fig. 8. Power control using the hierarchical control (dynamic performance).

the circuit breaker CB2 is closed to initiate the power transfer stage (Stage-III).

The performance of VFT during Stage-III is depicted in Figs. 8 and 9. According to power flow directions considered in Fig. 1, the positive value of $P^*_{\rm VFT}$ represents the power transferred from PN-I (stator side) to PN-II (rotor side) and negative quantity represents the reverse power flow.

The dynamic response of VFT during sudden changes in power transfer command ($P^*_{\rm VFT}$) is shown in Fig. 8. Initially, $P^*_{\rm VFT}$ is set equal to zero, and at t_3, it is changed from 0 to 0.85 p.u. It can be noticed that P_s and P_r reach the steady state ($P_s = P^*_{\rm VFT}$) within 3 s. Further to check the response of VFT during power reversal, $P^*_{\rm VFT}$ is changed from 0.85 to -0.85 p.u. at t_4. It can be observed that VFT reaches the new steady state within 3 s in this case as well. Note that, due to the active power loss in VFT there is a small difference between P_s and P_r during the steady state. The active power supplied/absorbed by the dc drive is governed by the direction of power transfer and it is observed around 0.5–0.7 p.u. (around 0.012–0.015 p.u. on VFT power base).

The expanded view of steady-state results for $P^*_{\rm VFT}$ equal to 0.85 and –0.85 p.u. is shown in Fig. 9 in Zoom1 and Zoom2, respectively. In Zoom1, it can be noticed that the stator current $i_{s,a}$ is nearly in-phase with stator voltage $v_{s,a}$ as the power is being transferred from PN-I to PN-II. Whereas in case of reverse power flow (Zoom2), $i_{s,a}$ is noticed to be almost out-of-phase with $v_{s,a}$. The change in Q_S and Q_r with the change in $P^*_{\rm VFT}$ (in Figs. 8 and 9) represents their uncontrolled nature as discussed in Section III-B. Due to this, the stator current ($i_{s,a}$) magnitudes are different for the same amount of active power flow in both directions. Note that the difference between Q_S and Q_r is almost constant as per (13) and is equal to the reactive power absorbed/required by VFT (Q_m).

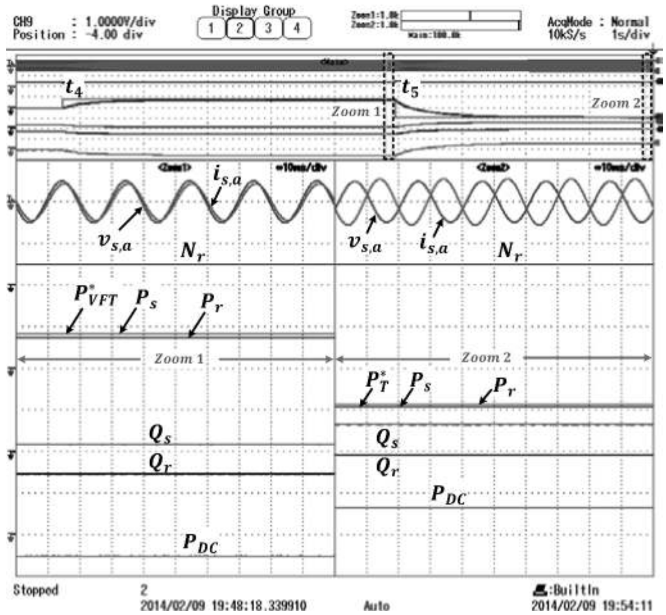

Fig. 9. Power control using the hierarchical control (steady-state performance).

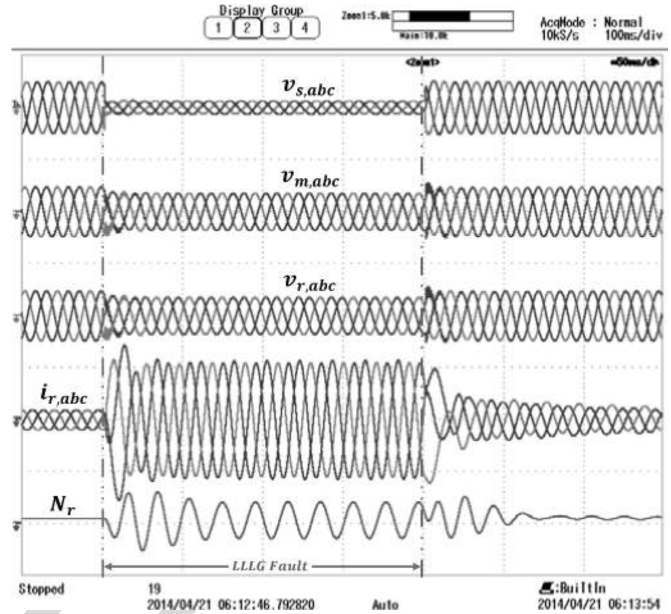

Fig. 11. VFT performance during three-phase fault in PN-I (stator side) without SDBR protection scheme.

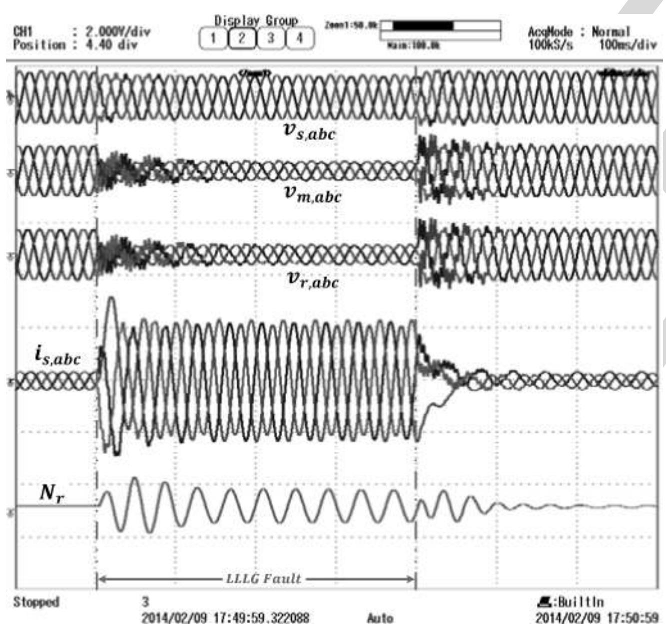

Fig. 10. VFT performance during three-phase fault in PN-II (rotor side) without SDBR protection scheme.

B. Fault Ride-Through Performance

The behavior of VFT without any additional FRT mechanism, during the three-phase grid fault at PN-II is shown in Fig. 10. The important variables that depict the fault propagation problem with VFT are shown in Fig. 10. These variables include: PN-I voltage at PCC-I ($v_{s,\mathrm{abc}}$: $1\ \mathrm{div} = 2\ \ $ p.u.), the PN-II voltage at PCC-II ($v_{m,\mathrm{abc}}$: $1\ \mathrm{div} = 2\ \ $ p.u.), the rotor voltage ($v_{r,\mathrm{abc}}$: $1\ \mathrm{div} = 2\ \ $ p.u.), current drawn from PN-I ($i_{s,\mathrm{abc}}$: $1\ \mathrm{div} = 5\ \ $ p.u.), and the rotor speed (N_r: $1\ \mathrm{div} = 5$ p.u.). Prior to the grid fault, the system is under steady state with a power transfer of 0.85 p.u. from PN-I to PN-II. A significant voltage dip in both PCC-II ($v_{m,\mathrm{abc}}$) and rotor ($v_{r,\mathrm{abc}}$) voltages and sudden rise in stator current ($i_{s,\mathrm{abc}}$) can be noticed during the grid fault condition. The rise in stator current signifies that the fault in the rotor side (PN-II) is propagated to the stator side (PN-I). The fault current in PN-I reaches 5 p.u. which may cause threat to PN-I security and reliability. Moreover, the large oscillations introduced in the rotor speed (N_r) during the grid fault causes the sustained mechanical vibrations that may destroy the WRIM and dc motor bearings.

The fault propagation from the stator side to rotor side during a grid fault on stator side (PN-I) is depicted in Fig. 11. It can be noticed that the rotor current rises 5 p.u. during the fault without SDBR protection. This signifies the fault propagation from PN-I to PN-II.

To avoid such high fault currents and mechanical stress due to fault propagation, the SDBR protection scheme shown in Fig. 4 is designed (explained in Section III). The set of specifications considered during the SDBR design are: $V_{\mathrm{fault\_min}} = 0.1$ pu, $V_{\mathrm{fault\_max}} = 0.9$ pu, $P_{\mathrm{rated}} = 0.85$ p.u, $k = 1.1$ and $V_{r\_\min} = 0.9$ pu. The values for $R_{\mathrm{SDBR\_max}}$ and $R_{\mathrm{SDBR\_min}}$ calculated using (14) and (15) are 4 Ω and 40 Ω, respectively. From (16), the SDBR resistance values computed are $R_1 = 4\ \Omega$, $R_2 = 12\ \Omega$, and $R_3 = 24\ \Omega$ respectively.

The performance of VFT with the proposed SDBR scheme during three-phase to ground fault on PN-II is shown in Fig. 12. Due to the activation of SDBR scheme during the three-phase fault, the rotor voltage ($v_{r,\mathrm{abc}}$) is restored to the nominal level and the stator current ($i_{s,\mathrm{abc}}$) is restricted to the maximum rated current. As the activation of SDBR does not allow the stator current to reach high value, it prevents the fault propagation through VFT. The oscillations in the speed are also reduced with

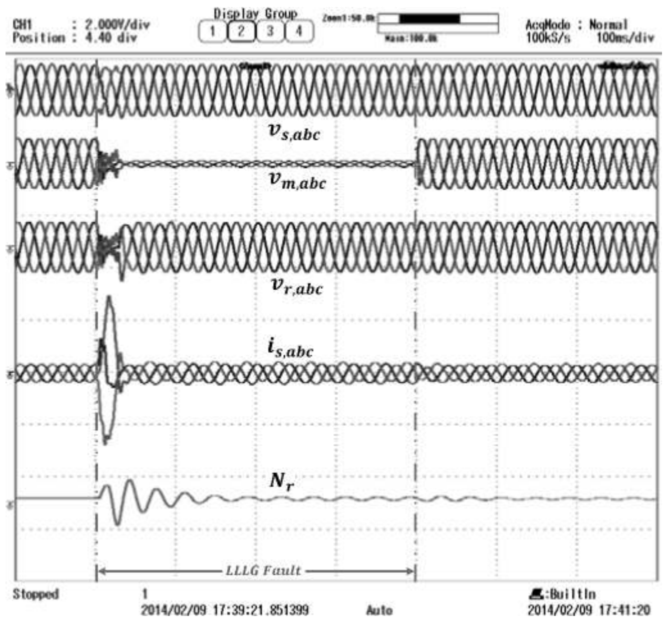

Fig. 12. VFT performance during three-phase fault in PN-II (rotor side) with the SDBR protection scheme.

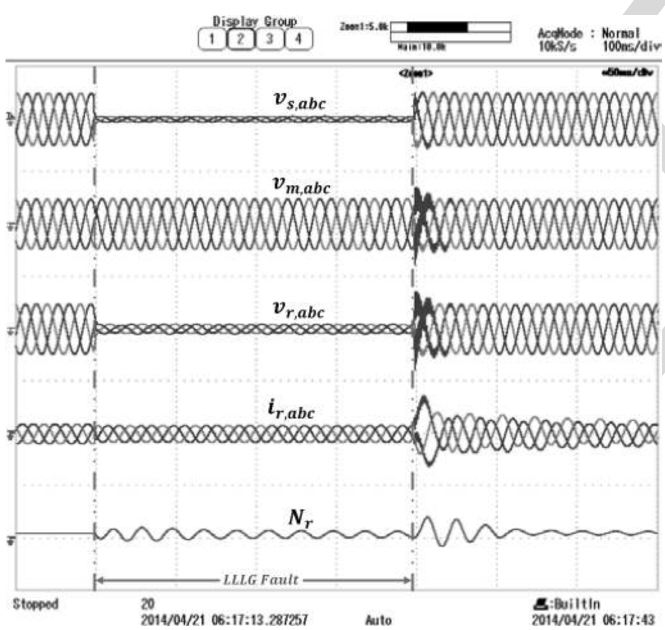

Fig. 13. VFT performance during three-phase fault in PN-I (stator side) with the SDBR protection scheme.

the SDBR and are damped out due to the presence of mechanical inertia and opposing torque produced by the dc motor drive.

The performance of VFT with the proposed SDBR protection scheme during the three-phase to ground fault on the stator side (PN-I) is depicted in Fig. 13. It can be observed that the grid fault on the stator side causes a sudden dip in stator voltage, $v_{s,\mathrm{abc}}$. During this condition, the insertion of SDBR series resistance on the rotor side brings down the $v_{r,\mathrm{abc}}$ without affecting $v_{m,\mathrm{abc}}$. This restricts the flow of fault current through VFT to a nominal level as noticed from $i_{r,\mathrm{abc}}$. Note that the rise in $i_{r,\mathrm{abc}}$ immediately after the fault clearance is mainly due to the sudden change in stator flux caused by the abrupt recovery of stator voltage.

The satisfactory performance during the steady-state, dynamic, and grid fault conditions proves that VFT with proposed SDBR scheme and hierarchical control strategy is a potential contender for the application of controlled power transfer between two asynchronous power networks.

VII. Conclusion

This paper presents a new hierarchical control strategy to control the VFT during normal and FRT operating conditions. This paper further investigates the possible fault propagation issue through VFT from one network to another. The SDBR-based FRT scheme has been proposed for VFT to mitigate the fault propagation. The detailed working principles of the VFT, all the stages of hierarchical control and FRT operation are verified using the real-time HIL system.

The detailed results under three stages of the proposed hierarchical control (frequency matching, phase angle matching, and power transfer control) during steady-state and dynamic conditions prove its comprehensiveness. The satisfactory results in limiting the fault propagation through VFT during the grid faults validate the effectiveness of SDBR protection scheme. In summary, along with the power transfer control function of VFT, added capability to limit the fault propagation and inherent natural damping capability will make VFT an ideal solution for the interconnection of micro grids in the future power systems.

References

[1] M. P. Bahrman, "Overview of HVDC transmission," in *Proc. Power Syst. Conf. Expo.*, 2006, pp. 18–23.
[2] A. Merkhouf, P. Doyon, and S. Uphadayay, "Variable frequency transformer—Concept and electromagnetic design evaluation," *IEEE Trans. Energy Convers.*, vol. 23, no. 4, pp. 989–996, Dec. 2008.
[3] E. Larsen, "A classical approach to constructing a power flow controller," in *Proc. IEEE Power Eng. Soc. Summer Meeting*, 1999, vol. 2, pp. 1192–1195.
[4] R. J. Piwko, E. V. Larsen, and C. A. Wegner, "Variable frequency transformer—a new alternative for asynchronous power transfer" in *Proc. IEEE Power Eng. Soc. Conf. Expo.*, Durban, Jul. 2005, pp. 393–398.
[5] B. Bagen, D. Jacobson, G. Lane, and H. M. Turanli, "Evaluation of the performance of back-to-back HVDC converter and variable frequency transformer for power flow control in a weak interconnection," presented at IEEE Power Eng. Soc. Gen. Meeting, Tampa, FL, USA , Jun. 24–28, 2007, pp. 1–6
[6] A. S. Abdel-Khalik, A. Elserougi, S. Ahmed, and A. Massoud, "Brushless doubly fed induction machine as a variable frequency transformer," in *Proc. 6th IET Int. Conf. Power Electron., Mach. Drives*, Mar. 2012. Q3
[7] A. H. El Din, M. A. Abdullah, and M. Ibrahim, "A Matlab/Simulink model to study the performance of the VFT for the interconnection of weak and strong AC grids," in *Proc. IEEE Int. Elect. Mach. Drives Conf.*, May 2011, pp. 1635–1640.
[8] E. T. Raslan, A. S. Abdel-Khalik, M. Abdulla, and M. Z. Mustafa, "Performance of VFT when connecting two power grids operating under different frequencies," in *Proc. 5th IET Int. Conf. Power Electron., Mach. Drives*, 19–21, Apr. 2010, pp. 1–6.
[9] G. Chen and X. Zhou, "Digital simulation of variable frequency transformers for asynchronous interconnection in power system," in *Proc. IEEE Power Eng. Soc. Transmiss. Distrib. Conf.*, 2005, pp. 1–6.

[10] L. Contreras-Aguilar and N. Garcia, “Accelerated time domain solution of VFT using the Poincaré map method with an embedded implicit integration algorithm” in *Proc. North Am. Power Symp.*, Calgary, Canada Sep. 2008, pp. 1–8.

[11] L. Contreras-Aguilar and N. Garcia, “Fast convergence to the steady state operating point of a VFT park using the limit cycle method and a reduced order model,” in *Proc. IEEE Power Eng. Soc. Gen. Meeting*, Calgary, Canada, Jul. 2009, pp. 1–5.

[12] L. Contreras-Aguilar and N. Garcia, “Steady-state solution of a VFT park using the Newton method and a reduced order model,” in *Proc. IEEE Power Tech.*, Bucharest, Rumania, Jun./Jul. 2009, pp. 1–6.

[13] L. Wang and L. Y. Chen, “Reduction of power fluctuations of a large scale grid-connected offshore wind farm using a variable frequency transformer,” *IEEE Trans. Sustain. Energy*, vol. 2, no. 3, pp. 226–234, Jul. 2011.

[14] G. Poddar and V. T. Ranganathan, “Direct torque and frequency control of double-inverter-fed slip-ring induction motor drive,” *IEEE Trans. Ind. Electron.*, vol. 51, no. 6, pp. 1329–1337, Dec. 2004.

[15] P. Marken, J. Roedel, D. Nadeau, D. Wallace, and H. Mongeau, “VFT maintenance and operating performance,” in *Proc. Power Eng. Soc. Gen. Meeting Convers. Del. Elect. Energy*, Jul. 2008, pp. 1–5.

[16] D. Nadeau, “A 100-MW variable frequency transformer (VFT) on the Hydro-Quebec TransEnergie Network-the behavior during disturbance” in *Proc. Power Eng. Soc. Gen. Meeting*, Jun. 2007, pp. 1–5.

Bharath Babu Ambati received the B.E. degree in electrical and electronics engineering from the Sir C. R. Reddy College of Engineering (affiliated with Andhra University), Eluru, AP, India, in 2009; the M.Tech. degree in power electronics, electrical machines, and drives (PEEMD) from the Indian Institute of Technology (IIT) Delhi, New Delhi, India, in 2011; and is currently pursuing the Ph.D. degree in interdisciplinary engineering with the Masdar Institute of Science and Technology, Abu Dhabi, UAE.

From 2011 to 2012, he was with Schneider Electric India Private Limited as a Product Expert of Motion and Drives. His current research interests include power electronics, electrical machines, renewable energy generation, and power quality.

Parag Kanjiya received the B.Eng. degree in electrical engineering from the B.V.M. Engineering College, Sardar Patel University, V.V. Nagar, India, in 2009, and the M.Tech. degree in power systems from the Indian Institute of Technology Delhi (IITD), New Delhi, India, in 2011.

Since October 2011, he has been a Research Engineer with the Masdar Institute of Science and Technology, Abu Dhabi, UAE. His research interests include applications of power electronics in distribution systems, power quality enhancement, renewable energy, FACTS, and power system optimization.

Mr. Kanjiya was awarded the K.S. Prakasa Rao Memorial Award for earning the highest C.G.P.A at IITD in August, 2011.

Vinod Khadkikar (S’06–M’09) received the B.E. degree from the Government College of Engineering, Dr. Babasaheb Ambedkar Marathwada University, Aurangabad, India, in 2000; the M. Tech. degree from the Indian Institute of Technology (IITD), New Delhi, India, in 2002; and the Ph.D. degree from the École de Technologie Supérieure (ETS), Montréal, QC, Canada, in 2008, all in electrical engineering.

From December 2008 to March 2010, he was a Post-Doctoral Fellow at the University of Western Ontario, London, ON, Canada. From April 2010 to December 2010, he was visiting faculty at the Massachusetts Institute of Technology, Cambridge, MA, USA. Currently, he is an Associate Professor at the Masdar Institute of Science and Technology, Abu Dhabi, UAE. His research interests include applications of power electronics in distribution systems and renewable energy resources, grid interconnection issues, power quality enhancement, active power filters, and electric vehicles.

Dr. Khadkikar is currently an Associate Editor of the *IET Power Electronics Journal*.

Mohamed Shawky El Moursi (M’12) received the B.Sc. and M.Sc. degrees from Mansoura University, Mansoura, Egypt, in 1997 and 2002, respectively, and the Ph.D. degree from the University of New Brunswick (UNB), Fredericton, NB, Canada, in 2005, all in electrical engineering.

He was a Research and Teaching Assistant in the Department of Electrical and Computer Engineering, UNB, from 2002 to 2005. He joined McGill University as a Post-Doctoral Fellow with the Power Electronics Group. He joined Vestas Wind Systems, Arhus, Denmark, in the Technology R&D Group with the Wind Power Plant Group. He was with TRANSCO, UAE, as a Senior Study and Planning Engineer, and seconded as a Faculty Member in the Faculty of Engineering, Mansoura University. He was a Visiting Professor at the Massachusetts Institute of Technology, Cambridge, MA, USA. He is currently an Associate Professor in the Electrical Engineering and Computer Science Department, Masdar Institute of Science and Technology. His research interests include power system, power electronics, FACTS technologies, system control, wind turbine modeling, wind energy integration, and interconnections.

He is serving as an Associate Editor for *IET Renewable Power Generation* and *IET Power Electronics Journals*.

James L. Kirtley Jr. (F’91) received the Ph.D. degree from the Massachusetts Institute of Technology (MIT), Cambridge, MA, USA, in 1971.

He has been with the Large Steam Turbine Generator Department General Electric, and with Satcon Technology Corporation. Currently, he is a Professor of Electrical Engineering at MIT.

Dr. Kirtley served as an Editor-in-Chief of the IEEE TRANSACTIONS ON ENERGY CONVERSION from 1998 to 2006, and continues to serve as Editor and as a Member of the Editorial Board of *Electric Power Components and Systems*. He was awarded the IEEE Third Millennium Medal in 2000 and the Nikola Tesla Prize in 2002. He is a Registered Professional Engineer in Massachusetts and is a member of the United States National Academy of Engineering.

QUERIES

Q1. Author: Please spell out of OPAL-RT, PID, FACTS and C.G.P.A.
Q2. Author: Please check whether the edit in the sentence starting: "The dc motor drive power . . . ." is ok.
Q3. Author: Please provide page range in Ref. [6].
Q4. Author: Please provide location details.
Q5. Author: Please check if the edits to the BIOS of author "Vinod Khadkikar" are ok.
Q6. Author: Please provide location details.
Q7. Author: Please provide field of study.
Q8. Author: Please provide location details.